COMMUN. MATH. SCI.
Vol. 20, No. 8, pp. 2069–2106

HETEROGENEOUS MULTISCALE METHODS FOR ROUGH-WALL LAMINAR VISCOUS FLOW*

SEAN P. CARNEY† AND BJÖRN ENGQUIST‡

Abstract. We develop numerical multiscale methods for viscous fluid flow over a rough boundary. The goal is to derive effective boundary conditions, or wall laws, through high resolution simulations localized to the boundary coupled to a coarser simulation in the domain interior following the framework of the heterogeneous multiscale method. Rigorous convergence of the coupled system is shown in a simplified setting. Numerical experiments illustrate the utility of the method for more general roughness patterns and far field flow conditions.

Keywords. Rough boundaries; multiscale methods; fluid dynamics.

AMS subject classifications. 65N22; 65N30; 76D0.

1. Introduction

Standard partial differential equations for viscous flow such as the Stokes and Navier-Stokes equations naturally have no-slip boundary conditions. The velocity vector $u = 0$ at the boundary.

The no-slip condition however can generate a large separation of scales in a problem. The analysis and simulation of fluid flows over rough surfaces, for example, is challenging because the no-slip condition generates boundary layers in the vicinity of the roughness whose resolution can be computationally expensive.

Surface roughness plays an important role in a variety of physical applications. In geophysical fluid dynamics, meteorological flows are known to be affected by mountain ranges, city landscapes, and wavy seas, while ocean currents are impacted by variations in the ocean floor as well as the coastline [45]. Rough surfaces can also effect a reduction in skin friction drag; the morphology of a swordfish's sword, shark dermal denticles, and riblets on the Stars and Stripes yacht in the 1987 America's Cup finals are all examples [14, 42]. In hypersonic flows, surface roughness is relevant because space shuttles typically contain periodic gaps between covering tiles designed for heat control [16]. Outside of fluid mechanics, electromagnetic wave scattering by an obstacle is known to depend on small-scale rugosity, or imperfections, along its surface [3].

In such cases where the no-slip condition either (i) is inaccurate or (ii) generates sharp boundary layers, it may be better in a computation to replace it with an effective boundary condition, or wall-law. Ideally, the wall-law captures the effect of the asymptotic small scales on the large scales. Computing in a domain without the small scale structure then results in a large reduction in the degrees of freedom necessary in a simulation.

Sometimes effective boundary conditions can be rigorously justified from first principles. Relevant to the present work is the Navier-slip law for viscous laminar flow. Other examples include the the Leontovitch boundary conditions for electromagnetic wave scattering, and the Beavers-Joseph-Saffman law for viscous, laminar flow over a

*Received: October 12, 2021; Accepted (in revised form): February 16, 2022. Communicated by Shi Jin.

†Department of Mathematics, University of California, Los Angeles, CA, 90095, USA (spcarney@math.ucla.edu).

‡Department of Mathematics and Oden Institute for Computational Engineering and Sciences, The University of Texas at Austin, Austin, TX, 78712, USA (engquist@oden.utexas.edu).

porous bed. There are other well-known wall-laws for which a theoretical justification is lacking, however. The logarithmic law-of-the-wall for wall-bounded turbulent flows [44, 46] and the electro-osmotic slip velocity (and associated zeta potential) for electrokinetic flows [50, 52] are two examples.

The focus here will be on viscous laminar flow over a rough boundary that varies with characteristic amplitude and period $0 < \epsilon \ll 1$. The problem is well understood mathematically and has been extensively analyzed with the tools of asymptotic homogenization theory. Rigorous estimates have been obtained for the linear, Stokes case [7], and for Poiseuille [33] and Couette [34] flows governed by the stationary Navier-Stokes equations in channel geometries with periodic roughness, as well as random, ergodic roughness [11, 17]. In Ref. [43] the authors obtain rigorous convergence results for more general, three-dimensional flows under the assumption that the solution to the corresponding problem with the no-slip boundary condition imposed along a smooth boundary possesses a smooth solution. Related mathematical studies also include [32] for channel flow over a porous bed, [13, 26] for meteorological flows, and [3, 4, 10] for Maxwell's equations.

There additionally exist several numerical studies of rough-wall viscous flow. Computational techniques based on domain decomposition [6] and asymptotic expansions [5] have been previously proposed for modeling the effect of surface roughness on the flow in the domain interior. Similar strategies have also been explored for compressible flows over rough surfaces [19] and for shape optimization with the purpose of minimizing drag for both laminar and turbulent incompressible flows, assuming the roughness is within the viscous sublayer [24, 25]. More recently, Bottaro and Naqvi [12] and Lācis, Bagheri, and coauthors [35, 54] used asymptotic expansions to develop high-order wall-laws for flows over rough surfaces and porous media, respectively. In the latter groups' work, wall-laws for rough surfaces are included as a limiting case.

The goal in this work is to derive the wall-law that describes the average effect of surface roughness on the large scale flow by local, high-resolution 'microscale' simulations. These are in turn coupled to a coarse-scale simulation in the interior following the framework of the heterogeneous multiscale method (HMM) [2, 22]. This 'macroscale' simulation will use the effective boundary condition along a smooth boundary.

The proposed method shares some features of classical domain decomposition and adaptive mesh refinement, however it is fundamentally different in that the classical methods try to resolve the ϵ-scale in the neighborhood of the rough boundary throughout the entire computational domain, while here local refinement is only used selectively to derive effective boundary conditions. The domain size of the local simulations scales with ϵ, and hence the overall numerical degrees of freedom are independent of ϵ. The overall computational cost is thus drastically reduced compared to a full discretization of the problem.

The existing mathematical homogenization theory for viscous, rough-wall flow justifies an effective boundary condition of Robin-type for the case of periodic or random, stationary ergodic roughness. Guided by the theory, the wall-law in the proposed method is also a Robin condition; however the method is designed to be applicable to general roughness profiles, so long as there is a separation of scales between the roughness characteristics and the size of the full domain.

For the case of Stokes flow in a channel with periodic roughness, we exploit linearity to prove several properties of the proposed method. We first show that a back-and-forth iteration used to solve the coupled macro/microscale system converges to a fixed point, and that the resulting wall-law leads to a coercive macroscale problem. Moreover, we

show the convergence happens rapidly; the coefficients in the wall-law produced by the first and second iterations differ by less than $\mathcal{O}(\epsilon^2)$. Finally, we show that the macroscale approximation produced by the HMM and the true rough-wall flow both limit to the same quantity as ϵ vanishes. We do not show, however, any rigorous estimates relating the HMM approximation to the true rough-wall flow, as the creation of new results in homogenization theory is outside of the scope of the present work.

The structure of the paper is as follows. Section 2 provides background first for the problem of laminar, viscous flow over a rough boundary and then for the heterogeneous multiscale method. Included is a brief asymptotic analysis of the problem that slightly modifies that of Achdou et al. [5]. The asymptotics motivate the form of the effective boundary condition used in Section 3, where the heterogeneous multiscale method is proposed and analyzed. Numerical results in Section 4 illustrate the method accurately and efficiently captures the average effect of surface roughness both where the homogenization theory is applicable and in more general settings. Finally, Section 5 contains some concluding remarks.

2. Background

There exists a large amount of mathematical results available in the literature concerning the asymptotic behavior of laminar incompressible flow in the presence of a rough boundary of characteristic height and wavelength ϵ; see [4–7, 11, 17, 33, 34, 54], mentioned in the introduction, as well as references therein. Although there are differing physical assumptions and levels of mathematical rigour associated to each work, all justify the use of a Robin-type condition on a smooth boundary near the original rough boundary. If u_τ denotes the fluid velocity vector tangential to the smooth boundary, and n denotes the unit vector normal to the boundary, the wall-law is of the form

$$u_\tau = \alpha \nabla u_\tau \cdot n. \tag{2.1}$$

This is typically coupled with the no-penetration condition $u \cdot n = 0$. In the available homogenization theory, either periodic roughness or random, stationary ergodic roughness is assumed. Furthermore, the smooth boundary is assumed to be flat; it aligns with a coordinate axis and exhibits no curvature. In these settings, the slip amount α is a constant given by the average of a local corrector that decays exponentially fast in the wall-normal variable. In more general situations, however, it should be noted that α could exhibit tangential variations.

Regardless of whether or not α is constant or varies tangentially, in two dimensions it is a scalar value. In three dimensions, however, it could more generally be a tensor. We focus in this work on the two-dimensional case for ease of exposition and so that numerical examples of the full, rough-wall problem are feasible on a workstation. All that follows, however, can be readily generalized to three dimensions, and Remark 3.3 in Section 3 briefly describes how our scheme generalizes to this case.

To see how a wall-law of the form (2.1) can arise, we now briefly conduct formal asymptotic analysis of two-dimensional, viscous laminar flow in rough domain. The analysis is nearly identical to that of Achdou et al. [5], and below we quote two of their theorems relevant to current work. In particular the asymptotics lead to the same linear cell problem whose solution is the first order corrector in the asymptotic expansion. After scaling by the small-scale parameter ϵ, the coefficient α in (2.1) then is simply the average of this solution.

There are two differences. The first is that we consider a rough boundary parameterized by the product of a rapidly oscillating periodic function φ^ϵ and a slowly varying function β. This simply results in the modulation of the slip-amount by β. The second

difference is that the authors in [5] consider high Reynolds number (Re) stationary flow, where Re is proportional to $1/\epsilon$. Since such flows are expected to be sensitive to turbulent instabilities in the presence of rough boundaries on physical grounds, we consider the asymptotic regime of low Reynolds number flow. The low Re case is additionally in line with the more rigorous analysis in [11,33,34].

We preface the asymptotics with some definitions to be used throughout the paper.

2.1. Preliminary definitions. First, let e_1 and e_2 be the standard unit vectors in $\mathbb{R}^2$, and let x_1 and x_2 parameterize the horizontal and vertical directions as in Figure 2.2.

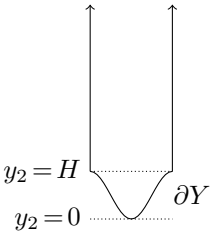

FIG. 2.1. *Semi-infinite domain Y with lower boundary $\partial Y = \{(y_1, y_2) \in [0,1) \times \mathbb{R} \,|\, y_2 = \varphi(y_1)\}$ for some periodic function φ.*

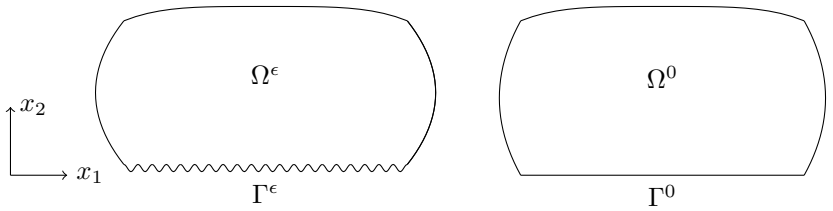

FIG. 2.2. *Domain Ω^ϵ with periodic, sinusoidal roughness and corresponding Ω^0 with flat boundary.*

Let $\varphi : \mathbb{R} \to \mathbb{R}$ be a bounded, Lipschitz continuous, periodic function with maximum value $H := \|\varphi\|_\infty$ that satisfies $\varphi(N) = H$ for every $N \in \mathbb{Z}$, and $\varphi(t+1) = \varphi(t) \geq 0$ $\forall t \in \mathbb{R}$. Let ϵ be some fixed small parameter, $0 < \epsilon \ll 1$, and define $\varphi^\epsilon(x_1) := \epsilon\varphi(x_1/\epsilon)$. For smooth, bounded function $\beta : \mathbb{R} \to \mathbb{R}$ that is independent of ϵ, define $\zeta^\epsilon(x_1) := \beta(x_1)\varphi^\epsilon(x_1)$ to be the function that parameterizes the rough boundary. Without loss of generality, assume that $\|\beta\|_\infty = 1$ for ease of exposition below. Further assume that β is bounded below by a positive constant, so that $\beta \geq \beta_* > 0$ and hence $\zeta^\epsilon(x_1) \geq 0$ $\forall x_1 \in \mathbb{R}$.

Let $Y = \{(y_1, y_2) \in [0,1) \times \mathbb{R} |\, y_2 \geq \varphi(y_1)\}$ be a domain containing a periodic "cell" of φ, semi-infinite in the vertical direction with lower boundary $\partial Y = \{y \in [0,1) \times \mathbb{R} | y_2 = \varphi(y_1)\}$; for example, see Figure 2.1. Let $L^2_{\text{per}}(Y)$ be the space of square integrable functions in Y that are 1-periodic in the y_1 variable, and let $H^1_{\text{per}}(Y) \subset L^2_{\text{per}}(Y)$ be the subspace whose first derivatives also belong to $L^2_{\text{per}}(Y)$. Also, let $\mathcal{S}_{\text{per}}(Y) \subset L^2_{\text{per}}(Y)$ be the subspace of functions that decay exponentially fast in y_2, as well as all of their derivatives.

Let $\Theta^\epsilon = \{(x_1, x_2) \in \mathbb{R}^2 |\, x_2 \geq \zeta^\epsilon(x_1)\}$ be the semi-infinite domain contained in the upper half plane $x_2 \geq 0$ in $\mathbb{R}^2$, and let Ω be a bounded domain in $\mathbb{R}^2$ made of one piece

that intersects the line $\{x_2 = 0\}$. Take $\Omega^0 = \Omega \cap \{x_2 \geq 0\}$, and let $\Gamma^0 = \partial\Omega^0 \cap \{x_2 = 0\}$. Finally, take $\Omega^\epsilon := \Theta^\epsilon \cap \Omega^0$, so that Ω^ϵ has a rough boundary Γ^ϵ with characteristic amplitude and wavelength ϵ; for example, see Figure 2.2. Note that $\overline{\Omega^\epsilon} \to \overline{\Omega^0}$ as $\epsilon \to 0$.

2.2. Asymptotic analysis. Given Ω^ϵ, consider the following stationary Navier-Stokes problem

$$\begin{aligned} \mathcal{L}(u^\epsilon, p^\epsilon) := -\nu\Delta u^\epsilon + u^\epsilon \nabla u^\epsilon + \nabla p^\epsilon &= f \qquad \text{in } \Omega^\epsilon \\ \nabla \cdot u^\epsilon &= 0 \qquad \text{in } \Omega^\epsilon \\ u^\epsilon &= 0 \qquad \text{on } \partial\Omega^\epsilon \end{aligned} \tag{2.2}$$

where $\nu = \mathcal{O}(1)$. Other combinations of well-posed boundary conditions are possible, so long as the no-slip condition $u^\epsilon = 0$ is imposed on the rough wall Γ^ϵ.

First consider the approximation (u^0, p^0) that satisfies

$$\begin{aligned} \mathcal{L}(u^0, p^0) &= f \qquad \text{in } \Omega^0 \\ \nabla \cdot u^0 &= 0 \qquad \text{in } \Omega^0 \\ u^0 &= 0 \qquad \text{on } \partial\Omega^0. \end{aligned}$$

A simple Taylor expansion shows that the error along the rough boundary Γ^ϵ is $\mathcal{O}(\epsilon)$; indeed let $x^0 \in \Gamma^0$, $x^0 + \zeta^\epsilon(x_1^0)e_2 \in \Gamma^\epsilon$. Then

$$\begin{aligned} u^0\left(x^0 + \zeta^\epsilon(x_1^0)e_2\right) &= u^0(x^0) + \zeta^\epsilon(x_1^0)\frac{\partial u^0}{\partial x_2}(x^0) + \frac{1}{2}\left(\zeta^\epsilon(x_1^0)\right)^2 \frac{\partial^2 u^0}{\partial x_2^2}(\xi(x^0)) \\ &= \epsilon\beta(x_1^0)\varphi(x_1^0/\epsilon)\frac{\partial u^0}{\partial x_2}(x^0) + \mathcal{O}(\epsilon^2). \end{aligned} \tag{2.3}$$

The error can be improved by considering a higher order approximation that accounts for the geometry of the rough boundary.

Consider next the approximations

$$\begin{aligned} u^\epsilon(x) &\approx u^1(x) + \epsilon u_{BL}^1(x, x/\epsilon) = u^1(x) + \epsilon\beta(x_1)\frac{\partial u_1^1}{\partial x_2}(x_1, 0)\left(\chi(x/\epsilon) - \overline{\chi}e_1\right) \\ p^\epsilon(x) &\approx p^1(x) + p_{BL}^1(x, x/\epsilon) = p^1(x) + \beta(x_1)\frac{\partial u_1^1}{\partial x_2}(x_1, 0)\pi(x/\epsilon), \end{aligned} \tag{2.4}$$

where (u^1, p^1) satisfy

$$\begin{aligned} \mathcal{L}(u^1, p^1) &= f \qquad \text{in } \Omega^0 \\ \nabla \cdot u^1 &= 0 \qquad \text{in } \Omega^0 \\ u^1(x) - \epsilon\beta(x_1)\overline{\chi_1}\frac{\partial u_1^1}{\partial x_2}(x)e_1 &= 0 \qquad x \in \Gamma^0 \\ u^1 &= 0 \qquad \text{on } \partial\Omega^0 \setminus \Gamma^0. \end{aligned} \tag{2.5}$$

The constant $\overline{\chi_1}$ in the slip boundary condition posed along Γ^0 is defined to be the horizontal average of the horizontal component of the vector χ at $y = H$, that is, just above the roughness φ:

$$\overline{\chi_1} = \int_0^1 \chi_1(y_1, H)\, dy_1.$$

The pair (χ,π) satisfy

$$\begin{aligned} -\mu\Delta_y\chi+\nabla_y\pi&=0 && \text{in } Y\\ \nabla_y\cdot\chi&=0 && \text{in } Y\\ \chi(y)&=-\varphi(y_1) && y\in\partial Y\\ \chi-\overline{\chi}&\in H^1_{\text{per}}(Y)\\ \pi&\in L^2_{\text{per}}(Y) \end{aligned} \tag{2.6}$$

and hence only depend on the roughness geometry.

Another Taylor expansion shows that indeed $u^1+\epsilon u^1_{BL}$ is $\mathcal{O}\left(\epsilon^2\right)$ along Γ^ϵ, i.e. one order higher than u^0 as desired. Using the formal differentiation rule

$$\nabla\Phi(x,x/\epsilon)=\nabla_x\Phi(x,y)+\frac{1}{\epsilon}\nabla_y\Phi(x,y),$$

inserting the approximations (2.4) into $\mathcal{L}$, and using (2.5) and (2.6) give that the approximations (2.4) are $\mathcal{O}(\epsilon)$ pointwise in Ω^0.

The first theorem we quote from [5] asserts that the so-called cell-problem (2.6) has a unique solution that decays exponentially in y_2, and that $\overline{\chi_2}=0$. This means the influence of the correctors u^1_{BL} and p_{BL} in (2.4) are only asymptotically felt in a $\mathcal{O}(\epsilon\log(1/\epsilon))$ neighborhood of the rough boundary Γ^ϵ.

THEOREM 2.1 (Achdou et al. [5]). *There exists a unique pair of functions (χ,π) and a unique vector $\overline{\chi}\in\mathbb{R}^2$ such that $\chi-\overline{\chi}\in\left(H^1_{\text{per}}(Y)\right)^2\cap\left(\mathcal{S}_{\text{per}}(Y)\right)^2$, $\pi\in L^2_{\text{per}}(Y)\cap\mathcal{S}_{\text{per}}(Y)$ and (2.6) is satisfied in a weak sense. Furthermore, $\overline{\chi}$ is horizontal,*

$$\overline{\chi}=\overline{\chi_1}e_1.$$

The second quoted theorem provides a bound on the size of the constant $-\overline{\chi_1}$ and is crucial for the well posedness of the effective problem (2.5) and hence for its numerical approximation as well.

THEOREM 2.2 (Achdou et al. [5]). *Let $H:=\max_{y\in\partial Y}y=\|\varphi\|_\infty$. Then the constant $-\overline{\chi_1}$ satisfies the bound*

$$0\le-\overline{\chi_1}\le H.$$

As a result, the problem (2.5) is generally ill-posed; its variational form contains the term

$$\frac{\mu}{\overline{\chi}}\int_{\Gamma^0}u^1_1v_1/\beta\,ds$$

where v is some test function, which is not coercive when $\overline{\chi}<0$. For this reason, the effective boundary condition is posed just *above* the roughness, as oppposed to at $y=0$. This is consistent with location of the effective boundary condition in the more rigorous studies [11, 33, 34]. For any $\delta>\epsilon H$, the problem (2.5) becomes

$$\begin{aligned} \mathcal{L}(u^1,p^1)&=f && \text{in } \Omega^0_\delta\\ \nabla\cdot u^1&=0 && \text{in } \Omega^0_\delta\\ u^1(x)-\beta(x_1)(\epsilon\overline{\chi}+\delta)\frac{\partial u^1_1}{\partial x_2}(x)&=0 && x\in\Gamma^0_\delta \end{aligned}$$

$$u^1 = 0 \qquad \text{on } \partial\Omega_\delta^0 \setminus \Gamma_\delta^0,$$

where

$$\Omega_\delta^0 = \Omega^0 \cap \{x_2 \geq \delta\}, \qquad \Gamma_\delta^0 = \{x + (0,\delta), x \in \Gamma^0\}. \tag{2.7}$$

For this reason, the wall-law determined by the multiscale method described in Section 3 is likewise imposed just above the surface roughness.

2.3. Heterogeneous multiscale method. The heterogeneous multiscale method (HMM) is a general framework for designing multiscale algorithms that aims to capture the macroscopic behavior of a system without resolving the microscopic details in their entirety. Under the assumption of scale separation in the underlying physical system, HMM couples macroscopic simulations to local, microscopic simulations so that the simulation has an overall computational complexity independent of the fine scale. Comprehensive introductions to and reviews of HMM can be found in [2, 21, 22]; below we briefly describe the main idea of the method and its applicability to designing effective boundary conditions for fluid simulations.

Suppose there is a general model for the macroscopic state of a physical system that can be expressed as $M(\Psi, D) = 0$, where D represents the macroscopic data necessary for the model to be complete. Then the main goal of HMM is to approximate D by solving microscale problems locally in space and/or time that are constrained by the macroscopic solution. If the microscale problem is denoted by $m(\psi, d) = 0$, where the data d represents the input from the macroscopic system, then the HMM can be succinctly expressed as

$$\begin{aligned} M(\Psi, D) &= 0, \qquad & D &= D(\psi) \\ m(\psi, d) &= 0, \qquad & d &= d(\Psi). \end{aligned} \tag{2.8}$$

With a macroscopic solver in hand, the procedure is to first constrain the micro simulation to be consistent with local macro data: $d = d(\Psi)$. After solving for ψ in the micro domain, the missing macro data is estimated using the results from the micro simulation: $D = D(\psi)$.

The HMM framework has been utilized to compute effective boundary conditions for fluid simulation problems before. For instance, in [47, 48], the authors model fluid-fluid and fluid-solid interactions in which the standard no-slip boundary conditions for a continuum fluid are no longer accurate and must be inferred from microscopic models, such as molecular dynamics (MD). Using such a microscopic model throughout the entire computational domain is prohibitively expensive, due to the disparate spatial and temporal scales between the continuum and molecular dynamics involved. Instead, local molecular dynamic simulations are computed only along the interfaces for which a boundary condition is needed. In the language of (2.8) above, the macro-scale model M is Navier-Stokes equations, but the usual stress tensor is the missing data D to be replaced by a more accurate model coming from MD simulation where it is needed. The MD simulation is initialized to be consistent with the local values of the continuum velocity.

While not initially proposed as an example of HMM, the method of Superparameterization proposed by Grabowski [29] and developed by Majda and others [30, 39–41] is a multiscale method for the simulation of atmospheric flows that fits into the framework of HMM. The original idea of the method is to couple local computations for the turbulent transport quantities to a global macroscopic model for the atmosphere. The

local computations impose artificial scale separation in both space and time between the large scale energetic motions and the small scale fluctuations and hence allow for a reduced computational cost.

In the present setting of viscous laminar flow over a rough boundary, the macroscopic model M consists of the Navier-Stokes equations posed in domain with a smooth boundary. The missing data D necessary for the model to be complete is the coefficient in the wall-law (2.1) coming from the homogenization theory. The microscopic model m consists again of the Navier-Stokes equations, this time posed on a single "element" of roughness whose size is finite in the wall-normal direction. The constraint d is that the values of the microscopic solution variables ψ at the computational boundaries (those that are *not* the rough wall, where the no-slip condition is prescribed) must be consistent with the local values of the macroscopic flow variables Ψ at those locations. Once the microscopic problem is solved, the solution ψ is suitably averaged to estimate the slip amount D; in this way the models are formally coupled. This coupling is more fully detailed and analyzed below in Section 3.

3. HMM for viscous laminar flow over a rough boundary

After some preliminary definitions, we now describe a heterogeneous multiscale method (HMM) for the efficient computation of the effective boundary condition, or wall-law, for the case of laminar flow over a rough surface. We then discuss the details of its practical implementation and analyze some of its properties.

3.1. Preliminary definitions. Consider a translation of the domains Ω^ϵ and $\Omega^0_{\epsilon H}$ defined in Section 2.1 and (2.7) by ϵH units in the negative x_2 direction, where $H = \|\varphi\|_\infty$ as before, so that

$$(x_1, x_2) \mapsto (x_1, x_2 - \epsilon H);$$

note that $\Omega^0_{\epsilon H} \subset \Omega^\epsilon$ still of course holds after the translation. Define Ω^{mac} to be the resulting translation of $\Omega^0_{\epsilon H}$, and for simplicity continue to refer to the translation of Ω^ϵ as Ω^ϵ (and similarly for the rough boundary Γ^ϵ). In addition, rename $\Gamma^0_{\epsilon H}$–the flat part of the boundary of Ω^{mac} defined by (2.7)–to be simply Γ.

Consider also a collection of points $\{s_1, s_2, \ldots, s_J\}$, each $s_j \in \mathbb{R}$, and assume $|s_j - s_{j+1}| \geq \epsilon$ for each j. Let $\{L_1^{\text{mic}}, L_2^{\text{mic}}, \ldots, L_J^{\text{mic}}\}$ be a collection of positive real values. Define the micro-domains Ω_j^{mic} to be the domains bounded by the curves $x_1 = s_j$ on the left, $x_1 = s_j + L_j^{\text{mic}}$ on the right, $x_2 = \gamma > 0$ above, and $\{(x_1, x_2) | x_2 = \zeta^\epsilon(x_1) - \epsilon H\}$ below. The lower curve is simply the portion of Γ^ϵ from $x_1 = s_j$ to $s_j + L_j^{\text{mic}}$. Note that of course ζ^ϵ need not agree at the locations s_j and $s_j + L_j^{\text{mic}}$. Denote this portion of the micro-domains $\partial\Omega^{\text{mic}}_{j,\text{noslip}}$, as this is where the physical wall is located. Denote the remaining portion of the boundary $\partial\Omega^{\text{mic}}_{j,\text{D}} = \partial\Omega_j^{\text{mic}} \setminus \partial\Omega^{\text{mic}}_{j,\text{noslip}}$, since the flow will generally satisfy some Dirichlet condition there. Lastly, assume γ and each L_j^{mic} are $\mathcal{O}(\epsilon)$. See Figure 3.1 for an example of such a configuration.

REMARK 3.1. In general, the HMM algorithm described below is not limited to rough domains with boundaries parameterized by oscillatory functions of the form $\zeta^\epsilon(x_1) = \beta(x_1)\varphi^\epsilon(x_1)$, i.e. rapidly oscillating periodic functions modulated by a slowly varying smooth function, as assumed in Section 2.1. In particular we note that the algorithm naturally adapts to different scalings for φ^ϵ than the one assumed in asymptotic analysis of Section 2.2, e.g. $\varphi^\epsilon = \epsilon\varphi(x_1)$ or $\varphi^\epsilon = \varphi(x_1/\epsilon)$.

REMARK 3.2. For the micro-domain problems defined below to be well-posed, the corners of the Ω_j^{mic} domains should be mollified; such technical details are not considered

here.

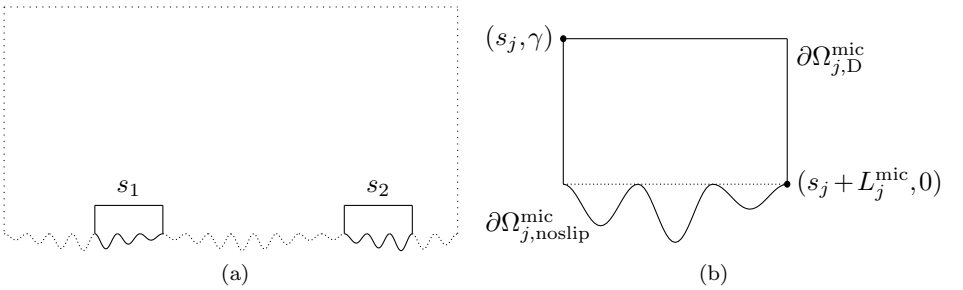

FIG. 3.1. *(a) Example domain Ω^ϵ (·····) containing several Ω^{mic}_j (—). (b) One instance of a micro domain Ω^{mic}_j whose boundary consists of two pieces, $\partial\Omega^{\text{mic}}_{j,\text{D}}$ and $\partial\Omega^{\text{mic}}_{j,\text{noslip}}$.*

3.2. Multiscale method. Let u^ϵ be a solution to the stationary Navier-Stokes equations in a domain Ω^ϵ with a rough-boundary. The purpose of the multiscale method is to efficiently produce an approximation U to the true, oscillatory flow u^ϵ by enforcing that U satisfy a wall-law of the form from the homogenization theory

$$U = \alpha \frac{\partial U_1}{\partial x_2} e_1 \tag{3.1}$$

on Γ, the boundary of the smooth domain Ω^{mac}. The coefficient α in the wall-law parameterizes the approximation and, in the language of HMM from Section 2.3, is the missing data D needed to complete the macro-scale model of u^ϵ.

The strategy utilized in [5] to determine α in the case of periodic roughness results from the asymptotic analysis from Section 2. One simply precomputes the solution χ to the (truncated) cell problem (2.6) and then takes the average of the horizontal component $\overline{\chi_1}$. After scaling by ϵ, this constant (plus some amount $\delta > \epsilon H$, in light of Theorem 2.2) is then taken to be the missing data α. The precomputing step is possible because the cell problem depends only on the geometry of the roughness.

In contrast, the multiscale method defined below to estimate α generally involves coupling a Navier-Stokes system posed in the macroscale domain Ω^{mac} to J separate Navier-Stokes systems posed in microscale domains Ω^{mic}_j, $1 \le j \le J$. Similar to the cell problem from the homogenization theory, the microscale systems account for the geometry of the rough surface, however, the current method is not restricted to domains with periodic roughness. The micro-systems are additionally constrained to match the averaged local flow values of the macroscale system, which could allow for a more accurate representation of the effect of surface roughness on the local macroscopic flow. In each Ω^{mic}_j, the ratio of the average flow and the average flow gradient (the shear) is computed. These values are interpolated along Γ, and the resulting function is then used for the slip amount α in (3.1).

We define first the macro and microscale systems, as well as a projection, smoothing, and interpolation operator before fully formulating the coupled multiscale model.

DEFINITION 3.1 (Macroscale system). *Let $M(U,P,\alpha)$ define the following PDE system posed in Ω^{mac} and parameterized by the slip amount α:*

$$-\nu\Delta U + U\nabla U + \nabla P - f = 0, \qquad \text{in } \Omega^{\text{mac}}$$

$$\begin{aligned} \nabla \cdot U &= 0, && \text{in } \Omega^{\text{mac}} \\ U - \alpha \frac{\partial U_1}{\partial x_2} e_1 &= 0, && \text{on } \Gamma \\ U &= 0, && \text{on } \partial\Omega^{\text{mac}} \setminus \Gamma \end{aligned}$$

Note that in general α can vary along Γ so that $\alpha = \alpha(x_1)$.

DEFINITION 3.2 (Microscale system). *Let $m_j\left(u^j, p^j, \Upsilon_j\right)$ define the PDE system posed in Ω_j^{mic} and parameterized by the Dirichlet boundary condition $\Upsilon_j : \partial\Omega_{j,\text{D}}^{\text{mic}} \to \mathbb{R}^2$:*

$$\begin{aligned} -\nu\Delta u^j + u^j \nabla u^j + \nabla p^j - f &= 0, && \text{in } \Omega_j^{\text{mic}} \\ \nabla \cdot u^j &= 0, && \text{in } \Omega_j^{\text{mic}} \\ u^j &= \Upsilon_j, && \text{on } \partial\Omega_{j,\text{D}}^{\text{mic}} \\ u^j &= 0 && \text{on } \partial\Omega_{j,\text{noslip}}^{\text{mic}}. \end{aligned}$$

For well-posedness, i.e. conservation of mass, Υ_j should satisfy

$$\int_{\partial\Omega_{j,\text{D}}^{\text{mic}}} \Upsilon_j \cdot n \, ds = 0. \tag{3.2}$$

Furthermore, let $\{\sigma_n\}_{n=1}^{\infty} \in \partial\Omega_{j,\text{D}}^{\text{mic}}$ be some convergent sequence with limiting point $\sigma = (s_j, 0)$ or $\sigma = (s_j + L_j^{\text{mic}}, 0)$. Then Υ_j should also satisfy

$$\lim_{n\to\infty} \Upsilon_j(\sigma_n) = 0 \tag{3.3}$$

for consistency with the no-slip condition posed along $\partial\Omega_{j,\text{noslip}}^{\text{mic}}$.

DEFINITION 3.3 (Projection operator). *Let $\mathcal{P}_j$ be the collection of continuous maps from $C(\Omega^{\text{mac}}, \mathbb{R}^2)$ to $C\left(\partial\Omega_{j,\text{D}}^{\text{mic}}, \mathbb{R}^2\right)$, where $C(X,Y)$ denotes the set of continuous functions from X to Y. Then we say π_j is a projection operator if $\pi_j \in \mathcal{P}_j$ and $\pi_j(f)$ satisfies the properties (3.2) and (3.3) for any $f \in C(\Omega^{\text{mac}}, \mathbb{R}^2)$.*

This projection operator is the mechanism by which the micro-problems m_j are constrained to match the macroscopic solution U. Suppose that U is a continuous solution to $M(U, P, \alpha)$ for $\alpha \neq 0$. Note then that simply taking the trace of U along $\partial\Omega_{j,\text{D}}^{\text{mic}}$ is not sufficient to be a projection operator in the above sense; even though the conservation of mass property (3.2) holds, the constraint (3.3) will not because of the slip condition on Γ. A specific example of a projection map is mentioned in Remark 3.4 and more fully detailed in Appendix A.

DEFINITION 3.4 (Smoothing operator). *For continuous and integrable $\psi : \mathbb{R}^2 \to \mathbb{R}$ and $y \in \mathbb{R}$, define the operator*

$$\langle \psi \rangle_L (x, y) := \int_x^{x+L} \psi(s, y) \, ds$$

which integrates ψ in the horizontal direction along a L-sized strip $[x, x+L]$ at fixed height y.

DEFINITION 3.5 (Interpolation operator). *For $\{(s_j, \alpha_j)\}_{j=1}^{J} \in \mathbb{R}^{2\times J}$, let*

$$\mathcal{I}((s_1, \alpha_1), \ldots, (s_J, \alpha_J)) : \mathbb{R}^{2\times J} \to C(\Gamma)$$

denote a piecewise continuous polynomial interpolant based on the given points.

Using the above definitions, the HMM is formally defined as follows; given a roughness profile ζ^ϵ, macroscale domain Ω^{mac}, and a collection of points $\{s_j, L_j^{\text{mic}}\}_{j=1}^J$ with associated micro-domains Ω_j^{mic}, find $\big((U,P),(u^1,p^1),\dots,(u^J,p^J)\big)$ satisfying the coupled system of equations:

$$\begin{aligned} M(U,P,\alpha) &= 0 \\ m_j\left(u^j,p^j,\Upsilon_j\right) &= 0 \qquad 1 \le j \le J \end{aligned} \tag{3.4}$$

where

$$\begin{aligned} \Upsilon_j &= \pi_j(U) \qquad 1 \le j \le J, \\ \alpha &= \mathcal{I}((s_1,\alpha_1),\dots,(s_J,\alpha_J)), \end{aligned}$$

and

$$\alpha_j = \frac{\langle u_1^j \rangle_{L_j^{\text{mic}}}(s_j,0)}{\langle \partial u_1^j/\partial x_2 \rangle_{L_j^{\text{mic}}}(s_j,0)}, \qquad 1 \le j \le J. \tag{3.5}$$

The HMM thus consists of a stationary Navier-Stokes equation in Ω^{mac} with slip amount α and J stationary Navier-Stokes equations posed in the domains Ω_j^{mic}, each of which depend on the projection of U onto the boundaries $\Omega_{j,D}^{\text{mic}}$. Given a boundary condition Υ_j and corresponding micro-solution u^j, the slip amounts α_j are defined to be the ratio of the average horizontal flow velocity to the average flow derivative in the vertical direction. The average is taken across the length L_j of the micro-domain at $x_2 = 0$, i.e. just above the roughness.[1] The values $\{\alpha_j\}_{j=1}^J$ are patched together with some interpolation scheme $\mathcal{I}$ and in turn utilized by the macro-solver.

The formula (3.5) is directly inspired by the existing mathematical homogenization results, all of which say that there exists *some* α such that the Navier-slip condition relating u_1 and $\partial u_1/\partial x_2$ gives the correct asymptotic effect of surface roughness on the macroscale flow. Hence, we simply took the ratio (3.5) to be this α.

A natural question to ask given the form of the slip amount (3.5) is what happens in the case of vanishing flow gradient. For the case of a smooth, laminar flow, a near-wall Taylor expansion similar to (2.3) gives that $u_1(x_2) \sim x_2 \partial u_1/\partial x_2$, meaning that, if the flow gradient is small, so too must the flow velocity be small, effectively ruling out cases with slip amount α that blows up. Nevertheless, in general a situation with vanishing flow gradient could indeed lead to a possible breakdown of (3.5) for estimating α. For such cases, if the average flow gradient inside a micro domain is calculated to be smaller than some tolerance (whose numerical value perhaps may require some insight into the problem at hand), one could switch to using the Dirichlet condition $u = 0$ as the local effective boundary condition in the macro-solver.

REMARK 3.3 (Three-dimensional case). As mentioned in Section 2, the slip amount α in the wall-law (2.1) can generally be a tensor in the case of three-dimensional flow. Suppose (x_1,x_3) and x_2 denote the horizontal and vertical directions, respectively. Then

[1] In our numerical tests, we also considered computing the α_j values at some $x_2 \in (0,\gamma)$ and extrapolating the result back to $x_2 = 0$ for use in the macro-solver; see the discussion in Section 4.6 for the details.

the wall-law (2.1) for the macro-solver would be

$$U_i = \sum_{k\in\{1,3\}} \alpha_{ik} \frac{\partial U_k}{\partial x_2}, \qquad i = 1,3.$$

Each individual slip amount then is

$$(\alpha_j)_{ik} = \frac{\langle u_i^j \rangle_{L_j^{\mathrm{mic}}}(s_j,0)}{\langle \partial u_k^j/\partial x_2 \rangle_{L_j^{\mathrm{mic}}}(s_j,0)}, \qquad i,k \in \{1,3\},$$

where the index j runs over each micro-domain. Each entry is interpolated across the two-dimensional surface Γ to produce a slip amount α for the macro-solver.

REMARK 3.4 (Boundary conditions for the micro-systems). Given some macroscopic flow U, each of the microscopic problems depends on the boundary condition from the projection operator:

$$u^j = \Upsilon_j = \pi_j(U) \qquad \text{on } \partial\Omega_{j,\mathrm{D}}^{\mathrm{mic}}.$$

In the case when U is horizontal, i. e. the vertical component of the velocity vector is zero, or at least negligible compared with the horizontal component, then the boundary conditions for the micro-systems can be simplied to a "free stream" condition along the upper computational boundary $x_2 = \gamma$:

$$u^j = \frac{1}{L_j^{\mathrm{mic}}} \langle U_1 \rangle_{L_j^{\mathrm{mic}}}(s_j,\gamma)\, e_1 \tag{3.6}$$

and periodic boundary conditions at $x_1 = s_j$ and $x_1 = s_j + L_j^{\mathrm{mic}}$. In this case the projection operator π_j simply maps from $C(\Omega^{\mathrm{mac}},\mathbb{R}^2)$ to $\mathbb{R}$. Note that this approach is only practically feasible if the roughness function ζ^ϵ satisfies $\zeta^\epsilon(s_j) \approx \zeta^\epsilon(s_j + L_j^{\mathrm{mic}})$ so that a periodic mesh for the micro domain Ω_j^{mic} can be constructed without much error. In situations for which this is not true or when the macroscopic flow has a nontrivial vertical component, a more general approach is needed. We propose quadratic polynomial Dirichlet conditions for both the horizontal and vertical components of the velocity along each of the three faces $\partial\Omega_{j,D}^{\mathrm{mic}}$. Enforcing the no-slip condition, some interpolation constraints, and that the quadratic profiles preserve the macro-scale mass fluxes guarantees a unique, well-defined projection operator. The details can be found in Appendix A.

One key feature of the method clearly is the specification of the locations $\{s_j\}_{j=1}^J$ of the micro-domains Ω_j^{mic} and the domain lengths $\{L_j^{\mathrm{mic}}\}_{j=1}^J$. For Poiseuille type channel flow with periodic roughness, for instance, only one micro-domain covering a single periodic roughness element is necessary. In more realistic settings for which the surface roughness is nonperiodic and additionally varies over macroscopic length scales, the micro-domain lengths L_j^{mic} should be chosen large enough to cover a few of the estimated correlation lengths, or approximate periods. The s_j locations should also be placed frequently enough along Γ^ϵ to capture its large-scale, macroscopic variations. The numerical examples in Section 4 are chosen to approximate such situations.

3.3. Simulation algorithm. In Section 3.4, we use the contraction mapping principle to prove that the coupled, stationary system (3.4) has a unique solution for the simplified case of linear, Stokes flow in a channel with periodic roughness. In

practice, the coupled system is also solved iteratively starting from some initial guess for α. A simple choice is to use the no-slip condition along Γ, i.e. use $\alpha = 0$. One then solves the macroscale problem, estimates the boundary conditions for the microscale problems, computes their solution, and estimates an updated slip amount. This process is repeated until the difference between subsequent slip amounts is smaller than some prescribed tolerance.

More precisely, let $\tau > 0$ be some fixed tolerance, and let the macro/microscale domains Ω^{mac} and $\{\Omega_j^{\text{mic}}\}_{j=1}^J$ be given. Then:

(1) Let $\underline{\alpha} = 0$ and solve the macroscale problem

$$M(U, P, \underline{\alpha}) = 0 \qquad \text{for } (U, P).$$

(2) For each $j = 1, \ldots, J$ determine boundary conditions for the micro-domain $\Upsilon_j = \pi_j(U)$ and then solve the microscale problems

$$m(u^j, p^j, \Upsilon_j) = 0 \qquad \text{for } (u^j, p^j).$$

(3) For each $j = 1, \ldots, J$, estimate the local slip amounts

$$\alpha_j = \frac{\langle u_1^j \rangle_{L_j^{\text{mic}}}(s_j, 0)}{\langle \partial u_1^j / \partial x_2 \rangle_{L_j^{\text{mic}}}(s_j, 0)}$$

and then interpolate the values to define the a new slip amount

$$\alpha_{(0)} = \mathcal{I}((s_1, \alpha_1), \ldots, (s_J, \alpha_J)).$$

(4) If $\left\| \alpha_{(0)} - \underline{\alpha} \right\|_\infty < \tau$, compute a final macroscale solution (U, P) by solving

$$M(U, P, \alpha_{(0)}) = 0. \tag{3.7}$$

Otherwise, use (U, P) from (3.7), repeat steps (2) and (3) to produce a new $\alpha_{(1)}$, and compare $\alpha_{(1)}$ and $\alpha_{(0)}$. Repeat until successive slip amounts differ by less than the tolerance τ.

If the tolerance is set to $\mathcal{O}(\epsilon^2)$, we show in Theorem 3.2 that for the case of linear, Stokes flow in a channel with periodic roughness, the back-and-forth procedure just outlined will terminate in a single iteration. More precisely, we show $(\alpha_{(1)} - \alpha_{(0)})/\epsilon^2$ vanishes as $\epsilon \searrow 0$. For this case, the HMM hence requires only one solution of the microscale systems in practice; computing an updated slip amount $\alpha_{(2)}$ is not necessary. Although we have no proof for more general situations, we observe the same behavior in all the numerical experiments presented in Section 4. Despite the rapid convergence, the need to have some initial macro-flow U in hand from which to estimate boundary conditions $\Upsilon = \pi(U)$ for the micro-solvers is a disadvantage of the proposed HMM. In practice, the overhead cost to produce some initial Υ could for example be reduced by first computing U on a mesh that is relatively coarse.

For time-dependent problems, there is no need to find a fixed point between the macro and microscale systems; the back-and-forth procedure simply becomes a communication between two time-marching schemes. First, the macroscale system with slip amount α is integrated forward one macro-step ΔT in time. The updated U then fixes micro-domain boundary conditions $\Upsilon_j = \pi_j(U)$ for each j. The microscale system is integrated in time several micro-steps $N_{\text{mic}}\,\delta t \approx \Delta T$, after which a new slip amount α is estimated, and then the process repeats.

Finally, we note that since the microscopic systems $m_j(u^j, p^j, \Upsilon_j)$ are all independent of one another, they are trivially parallelizable.

3.4. Analysis of the the coupled system. We now prove some convergence results for our HMM in a simplified setting. Let $0<\gamma_1<\gamma_2<1$ and consider a macroscale channel configuration, so that $\Omega^{\text{mac}}=[0,l]\times[\gamma_1,1]$, where $0<\gamma_1<1$ and $l>0$. We assume the full channel with rough boundary that contains Ω^{mac} has periodic roughness with a maximum at $x_2=0$ as before. For technical reasons however we instead measure the slip amount in the micro-domain at $x_2=\gamma_1>0$, and hence impose the wall-law at this location in the macro-domain as well. This is consistent with Theorem 2.2 from Achdou et al. [5]. The micro-domain has height γ_2.

Let the fluid viscosity $\nu=1$ and assume both the macro and micro problems are driven by a constant forcing $f=-2e_1$ representing the macroscale pressure gradient forcing the flow.

For some fixed slip amount $\alpha>0$, a modified Poiseuille flow solves the stationary Navier-Stokes equations posed in Ω^{mac} with the no-slip condition $U=0$ at $y=1$ and the slip-condition $U=\alpha\,\partial U_1/\partial x_2\,e_1$ at $y=\gamma_1$:

$$U(x_2)=\left(-x_2^2+\left(\frac{\gamma_1^2-1-2\gamma_1\alpha}{\gamma_1-1-\alpha}\right)(x_2-1)+1\right)e_1.$$

Since the macro-flow is horizontal and the roughness is assumed to be periodic, the boundary condition for the micro-domain can be simplified to a free-stream condition at $x_2=\gamma_2$. We can thus define the map from the macro to microscale flow.

DEFINITION 3.6 (Macro $\longrightarrow$ micro map). *Let $\alpha\geq 0$ and define*

$$T_2(\alpha):=-\gamma_2^2+\left(\frac{\gamma_1^2-1-2\gamma_1\alpha}{\gamma_1-1-\alpha}\right)(\gamma_2-1)+1. \tag{3.8}$$

The derivative is

$$\frac{\partial T_2}{\partial\alpha}=(1-\gamma_2)\left(\frac{(\gamma_1-1)^2}{(\gamma_1-1-\alpha)^2}\right), \tag{3.9}$$

which is positive $\forall\alpha\geq 0$ and is guaranteed to be finite whenever $\alpha>0$.

Instead of the full nonlinear problem, we now consider a Stokes problem in the micro-domain Ω^{mic}

$$\begin{aligned}-\Delta u+\nabla p&=2e_1\\ \nabla\cdot u&=0\end{aligned} \tag{3.10}$$

with the boundary condtions $u=0$ along Γ_ϵ and $u=\mathcal{U}e_1$ at $x_2=\gamma_2$ for some $\mathcal{U}\in\mathbb{R}$. At the side-walls $\{x_1=0\}\times[0,\gamma_2]$ and $\{x_1=\epsilon\}\times[0,\gamma_2]$, (u,p) is periodic. Since all of the problem data is smooth, it is known [55] that u and p are smooth fields.

The linearity of the Stokes problem (3.10) allows us to decompose the micro solution into three pieces

$$u=u_1\big|_{\Omega_{\text{mic}}}+u_2+u_3, \tag{3.11}$$

which lets us systematically quantify the HMM slip amount α. The boundary conditions and domains for each piece are illustrated in Figure 3.2. We now describe each solution u_i, $i=1,2,3$ in more detail.

The first piece accounts for the constant forcing $-2e_1$ and is posed in the larger domain $[0,\epsilon]\times[-M,\gamma_2]\supset\Omega_{\text{mic}}$, where $M=\|\varphi^\epsilon\|_\infty=\epsilon H$ is the amplitude of the roughness.

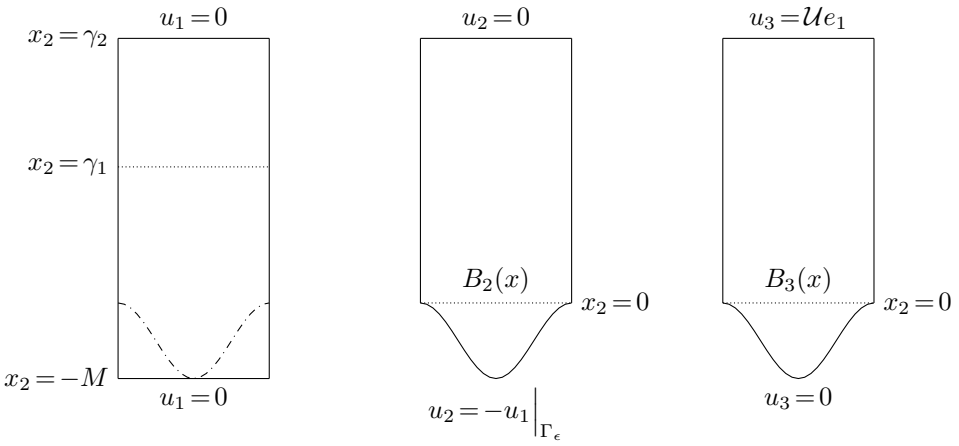

FIG. 3.2. *Boundary conditions for each of the three pieces making up the micro solution u. Each piece is additionally periodic at $x_1 = 0$ and $x_1 = \epsilon$. The interior traces of the second and third piece at the line $x_2 = 0$ are marked as $B_2(x)$ and $B_3(x)$.*

With no-slip at $x_2 = -M$ and $x_2 = \gamma_2$, it has analytic solution $u_1(x_2) = (x_2 + M)(\gamma_2 - y)e_1$ and $p_1 = 0$.

The second piece u_2 corrects for the fact that the restriction of u_1 to Ω^{mic} does not satisfy the no-slip condition along Γ_ϵ. It satisfies the homogeneous Stokes equations (i.e. without forcing), the no-slip condition at $x_2 = \gamma_2$ and

$$u_2 = -(u_1 \cdot e_1)\big|_{\Gamma_\epsilon} e_1$$

along Γ_ϵ. At this point and in the rest of the subsection, we abuse notation and refer to the *horizontal* component of the flow vector $u_i \cdot e_1$ simply as u_i for each $i = 1,2,3$.

Let $\langle \cdot \rangle(x_2)$ be shorthand for the integral operator $\langle \cdot \rangle_\epsilon(0, x_2)$ from Definition 3.4, and let $\overline{B}_2$ denote $\langle u_2 \rangle(0)$. Since $\langle u_2 \rangle(x_2)$ is independent of x_1, it satisfies a simple boundary value problem in $[0, \gamma_2]$ with solution

$$\langle u_2 \rangle(x_2) = -(\overline{B}_2/\gamma_2)x_2 + \overline{B}_2.$$

In Appendix B we show that in particular $|\overline{B}_2|/\epsilon \to 0$ as $\epsilon \searrow 0$.

The third piece u_3 will account for how the macro-solution U influences the micro-solution. It satisfies the no-slip condition along Γ_ϵ and the free stream condition $u_3 = \mathcal{U}$ at $x_2 = \gamma_2$. Like u_2 it is not externally forced, in contast to u_1. By linearity of the Stokes equation, $\langle u_3 \rangle(x_2)$ can be written as $\mathcal{U}\langle \tilde{u}_3 \rangle(x_2)$, where $\tilde{u}_3$ solves the same Stokes problem as u_3 but satisfies $\tilde{u}_3 = 1$ at $x_2 = \gamma_2$. Similar to $\langle u_2 \rangle(x_2)$, $\langle u_3 \rangle(x_2)$ can be written as

$$\langle u_3 \rangle(x_2) = \mathcal{U}\left(\frac{(1 - \tilde{B}_3)}{\gamma_2} x_2 + \tilde{B}_3\right)$$

where $\tilde{B}_3 = \langle \tilde{u}_3 \rangle(0)$. In Appendix B we show that $\tilde{B}_3 = \mathcal{O}(\epsilon)$.

Using the decomposition (3.11), we are now able to define the slip amount α given by (3.5) in the present setting. The slip amount is a map from the micro to macroscale flow.

DEFINITION 3.7 (Micro $\longrightarrow$ macro map). *Let $\mathcal{U} \in \mathbb{R}$ and define*

$$T_1(\mathcal{U}) := \frac{C_1 + C_2\mathcal{U}}{C_3 + (1-\tilde{B}_3)\mathcal{U}} \tag{3.12}$$

where

$$\begin{aligned} C_1 &= \epsilon\gamma_2(\gamma_1 + M)(\gamma_2 - \gamma_1) + \overline{B}_2(\gamma_2 - \gamma_1) \\ C_2 &= \tilde{B}_3(\gamma_2 - \gamma_1) + \gamma_1 \\ C_3 &= \epsilon\gamma_2(\gamma_2 - 2\gamma_1 - M) - \overline{B}_2, \end{aligned} \tag{3.13}$$

which is the ratio of the average of the horizontal component of the micro-flow u to the average of its derivative in the x_2 direction.

The derivative is

$$\frac{\partial T_1}{\partial \mathcal{U}} = \frac{\tilde{B}_3 C_1 + C_2 C_3 - C_1}{\Big((1-\tilde{B}_3)\mathcal{U} + C_3\Big)^2}.$$

The idea now is to prove the convergence of our multiscale method in the current simplified setting by first showing that the back-and-forth map T_2 composed with T_1 is a contraction for ϵ sufficiently small. Starting then from $\mathcal{U}_0 = T_2(\alpha)|_{\alpha=0}$, we'll show not only that sequence $(\mathcal{U}_n)_n$ generated by the back-and-forth iteration converges, but also that the slip-amount resulting from the limiting point is positive.

DEFINITION 3.8. *Let $T : \mathbb{R} \to \mathbb{R}$ be the nonlinear map given by the composition of the two maps defined by (3.8) and (3.12):*

$$T(\mathcal{U}) = T_2(T_1(\mathcal{U})).$$

From the chain rule

$$\frac{\partial T}{\partial \mathcal{U}}(\mathcal{U}) = \frac{\partial T_2}{\partial \alpha}(\alpha(\mathcal{U}))\frac{\partial T_1}{\partial \mathcal{U}}(\mathcal{U}),$$

and after some calculation one can show

$$\frac{\partial T}{\partial \mathcal{U}}(\mathcal{U}) = \frac{K_1(\gamma_1 - 1)^2(1-\gamma_2)}{K_2 + (1+K_3)\mathcal{U}} \tag{3.14}$$

where $K_1 = \tilde{B}_3 C_1 + C_2 C_3 - C_1$, $K_2 = C_1 + (1-\gamma_1)C_3$, and $K_3 = C_2 - \gamma_1 + \tilde{B}_3(\gamma_1 - 1)$.

We now prove T is a contraction map for all ϵ sufficiently small by showing $\partial T/\partial \mathcal{U}$ vanishes in the limit $\epsilon \searrow 0$ for all $\mathcal{U}$ larger than $T_2(\alpha)|_{\alpha=0}$. The result relies on an assumption that γ_2 is asymptotically larger than both ϵ and γ_1.

LEMMA 3.1. *Let $\mathcal{U}_0 = T_2(0)$, and assume that γ_1 and γ_2 monotonically tend to zero as $\epsilon \searrow 0$ as well as the quantities γ_1/γ_2 and ϵ/γ_2. Then $\forall \mathcal{U} \in [\mathcal{U}_0, \infty)$,*

$$\lim_{\epsilon \downarrow 0} \left| \frac{\partial T}{\partial \mathcal{U}} \right| = 0.$$

Proof. Equation (3.14) can be bounded as

$$\left| \frac{\partial T}{\partial \mathcal{U}} \right| \leq \frac{|K_1|}{|K_2 + (1+K_3)\mathcal{U}|}$$

$$= \frac{|K_1/\mathcal{U}|}{|K_2/\mathcal{U} + K_3 + 1|}.$$

Since $K_3 = \tilde{B}_3(\gamma_2 - 1) \to 0$ as $\epsilon \searrow 0$ by (B.3), then the result will follow if

$$\lim_{\epsilon \downarrow 0} K_i/\mathcal{U} = 0 \qquad \forall \mathcal{U} \in [\mathcal{U}_0, \infty)$$

for $i = 1,2$. Inserting the values of C_1, C_2, and C_3 into the expressions for each K_i, we see:

$$K_1/\mathcal{U}_0 = -\left[\tilde{B}_3\epsilon\gamma_1^2 - 2\tilde{B}_3\epsilon\gamma_1\gamma_2 + \tilde{B}_3\epsilon\gamma_2^2 - \epsilon\gamma_1^2 - M\epsilon\gamma_2 + \overline{B}_2\right]\gamma_2/\mathcal{U}_0$$

and

$$K_2/\mathcal{U}_0 = \left[-\epsilon\gamma_2^2 - \left(\epsilon\gamma_2^2 - \epsilon\gamma_2\right)M + \overline{B}_2(\gamma_2 - 1) - \left(\epsilon\gamma_1^2 - 2\epsilon\gamma_1\right)\gamma_2\right]/\mathcal{U}_0.$$

Note that $\mathcal{U}_0 = \gamma_2(1 + \gamma_1 - \gamma_2 - \gamma_1/\gamma_2)$, $M = \epsilon H$, and from the estimates in Appendix B we know both $\overline{B}_2/\gamma_2$ and $\tilde{B}_3$ vanish as ϵ tends to zero. Hence both K_1 and K_2 limit to 0 as $\epsilon \searrow 0$ based on the stated assumptions. Ergo, $\partial T/\partial \mathcal{U}$ also vanishes as ϵ tends to zero $\forall \mathcal{U} \in [\mathcal{U}_0, \infty)$. ∎

DEFINITION 3.9. *Let*

$$(\mathcal{U}_0, \mathcal{U}_1, \ldots, \mathcal{U}_n, \ldots)$$

be a sequence defined by $\mathcal{U}_0 := T_2(0)$ *and* $\mathcal{U}_{n+1} := T(\mathcal{U}_n)$ *for* $n \geq 0$. *Additionally define the sequence*

$$(\alpha_0, \alpha_1, \ldots, \alpha_n, \ldots),$$

where $\alpha_n := T_1(\mathcal{U}_n)$.

We can now prove the convergence of the HMM. We need an additional assumption, however, which places a limit on how close to $x_2 = 0$ one can theoretically take γ_1.

THEOREM 3.1. *Keeping the assumptions of Lemma 3.1, additionally assume*

$$\lim_{\epsilon \downarrow 0} \epsilon\gamma_2/\gamma_1 = 0. \tag{3.15}$$

Then $\exists \epsilon_0$ *such that* $\forall \epsilon$ *satisfying* $0 < \epsilon < \epsilon_0$, $\exists \mathcal{U}^*$ *to which* $(\mathcal{U}_n)_n$ *converges as* $n \to \infty$. *Moreover,* $\alpha^* := T_1(\mathcal{U}^*) > 0$.

The positivity of α^* is important to ensure the macroscopic problem with slip boundary condition remains coercive and can be compared to Theorem 2.2 from Achdou et al.

Proof. **(Proof of Theorem 3.1.)** By Lemma 3.1, T is a contraction map on $X := [\mathcal{U}_0, \infty)$. So, the fixed point iteration will converge so long as $\mathcal{U}_n \in X$ for each n. By the mean value theorem,

$$\mathcal{U}_{n+1} = T(\mathcal{U}_n) = T_2(\alpha_n) = \mathcal{U}_0 + \alpha_n \frac{\partial T_2}{\partial \alpha}(\xi_n), \qquad \forall n \geq 0 \tag{3.16}$$

for some $\xi_n \in (0, \alpha_n)$. Since $\partial T_2/\partial \alpha$ (given by (3.9)) is strictly positive and finite for $\alpha > 0$, the desired result will follow if it can be shown that $\alpha_n > 0$ for all n.

We first show $\alpha_0 > 0$, which implies $\mathcal{U}_1 > \mathcal{U}_0$ by (3.16). We then inductively assume $\mathcal{U}_n > \mathcal{U}_0$ for $n \geq 1$ and show that $\alpha_n > 0$ follows. Computing $\alpha_0 = T_1(\mathcal{U}_0) = T_1\big(\gamma_2(1+\gamma_1-\gamma_2-\gamma_1/\gamma_2)\big)$:

$$\begin{aligned}\alpha_0 &= \frac{C_1 + C_2\mathcal{U}_0}{C_3 + (1-\tilde{B}_3)\mathcal{U}_0} \\ &= \frac{\Big(M\epsilon\gamma_2 - \tilde{B}_3\gamma_1\gamma_2 + \epsilon\gamma_1\gamma_2 + \tilde{B}_3\gamma_2^2 + \tilde{B}_3\gamma_1 - \tilde{B}_3\gamma_2 + \gamma_1\gamma_2 - \overline{B}_2 - \gamma_1\Big)(\gamma_1-\gamma_2)}{M\epsilon\gamma_2 - \tilde{B}_3\gamma_1\gamma_2 + 2\epsilon\gamma_1\gamma_2 + \tilde{B}_3\gamma_2^2 - \epsilon\gamma_2^2 + \tilde{B}_3\gamma_1 - \tilde{B}_3\gamma_2 + \gamma_1\gamma_2 - \gamma_2^2 - \overline{B}_2 - \gamma_1 + \gamma_2}.\end{aligned} \tag{3.17}$$

Since $\gamma_1 < \gamma_2$, the numerator will be positive if

$$M\epsilon\gamma_2/\gamma_1 - \tilde{B}_3\gamma_2 + \epsilon\gamma_2 + \tilde{B}_3\gamma_2^2/\gamma_1 + \tilde{B}_3 - \tilde{B}_3\gamma_2/\gamma_1 + \gamma_2 - \overline{B}_2/\gamma_1 < 1.$$

Since $\tilde{B} = \mathcal{O}(\epsilon)$, the LHS of the inequality vanishes in the limit $\epsilon \searrow 0$ by the assumption (3.15). Thus the numerator is positive for ϵ sufficiently small. The denominator is positive if

$$1 > -M\epsilon + \tilde{B}_3\gamma_1 - 2\epsilon\gamma_1 - \tilde{B}_3\gamma_2 + \epsilon\gamma_2 - \tilde{B}_3\gamma_1/\gamma_2 + \tilde{B}_3 - \gamma_1 + \gamma_2 + \overline{B}_2/\gamma_2 + \gamma_1/\gamma_2.$$

Again by (3.15), the RHS vanishes as ϵ vanishes. Hence

$$\alpha_0 > 0$$

for ϵ sufficiently small.

Next, assume that $\mathcal{U}_n > \mathcal{U}_0$ for $n \geq 1$. We just showed that both the numerator $C_1 + C_2\mathcal{U}_0$ and denominator $C_3 + (1-\tilde{B}_3)\mathcal{U}_0$ in (3.17) are positive for ϵ sufficiently small. From the estimate (B.3) we know that both $1 - \tilde{B}_3 > 0$ and

$$C_2 > 0 \iff \tilde{B}_3\gamma_2/\gamma_1 - \tilde{B}_3 + 1 > 0,$$

are true for vanishing ϵ, from which we conclude

$$C_1 + C_2\mathcal{U}_n > C_1 + C_2\mathcal{U}_0 > 0$$

and

$$C_3 + (1-\tilde{B}_3)\mathcal{U}_n > C_3 + (1-\tilde{B}_3)\mathcal{U}_0 > 0.$$

This implies $\alpha_n > 0$.

By the method of induction, we conclude that for all ϵ sufficiently small, $\mathcal{U}_n \in X$ and $\alpha_n > 0$ $\forall n \geq 0$. Lemma 3.1 then guarantees the existence of a fixed point $\mathcal{U}^*$ such that $\mathcal{U}_n \to \mathcal{U}^*$ and $\mathcal{U}^* = T(\mathcal{U}^*)$. Furthermore, since $T_1(\mathcal{U})$ is continuous for $\mathcal{U} \in X$, we define the slip amount

$$\alpha^* = T_1(\mathcal{U}^*) = \lim_{n\to\infty} T_1(\mathcal{U}_n).$$

Since $(\mathcal{U}_n)_n$ is a convergent sequence, it must also be bounded. The inductive argument additionally showed the sequence is strictly increasing, meaning $\mathcal{U}_n < \mathcal{U}^*$ and hence $0 < C_3 + (1-\tilde{B}_3)\mathcal{U}_n < C_3 + (1-\tilde{B}_3)\mathcal{U}^*$ for all n. As just argued, we also have

$C_1 + C_2\mathcal{U}_n > C_1 + C_2\mathcal{U}_0 > 0$. Combining these inequalities shows that $(\alpha_n)_n$ is uniformly bounded below:

$$\alpha_n = \frac{C_1 + C_2\mathcal{U}_n}{C_3 + (1-\tilde{B}_3)\mathcal{U}_n} > \frac{C_1 + C_2\mathcal{U}_0}{C_3 + (1-\tilde{B}_3)\mathcal{U}^*} > 0.$$

Ergo $\alpha^* > 0$ as desired. ∎

Next we show that the slip-amount resulting from the fixed point iteration vanishes as ϵ limits to zero, ensuring the macroscale flow U will limit to a simple Poiseuille flow satisfying the no-slip condition along $x_2 = 0$. This is consistent with the limiting behavior of the true, rough-wall flow u^ϵ satisfying no-slip along Γ_ϵ.

COROLLARY 3.1. *Under the same assumptions as Theorem 3.1, we have*

$$\lim_{\epsilon \downarrow 0} \alpha^* = 0.$$

Proof. From the proof of Theorem 3.1 we know $\mathcal{U}_0 < \mathcal{U}^*$, so that

$$\alpha^* = T_1(\mathcal{U}^*) = \frac{C_1 + C_2\mathcal{U}^*}{C_3 + (1-\tilde{B}_3)\mathcal{U}^*} < \frac{C_1 + C_2\mathcal{U}^*}{C_3 + (1-\tilde{B}_3)\mathcal{U}_0}.$$

Using $\mathcal{U}_0 = \gamma_2(1 + \gamma_1 - \gamma_2 - \gamma_1/\gamma_2)$ the RHS of the inequality can be written

$$\frac{C_1/\gamma_2 + C_2/\gamma_2\mathcal{U}^*}{C_3/\gamma_2 + (1-\tilde{B}_3)(1 + \gamma_1 - \gamma_2 - \gamma_1/\gamma_2)}; \tag{3.18}$$

from the definitions (3.13) and bounds (B.2) and (B.3), it is clear (3.18) will vanish as $\epsilon \to 0$ so long as $\mathcal{U}^*$ is finite in the limit.

From (3.16) we have

$$\mathcal{U}^* = \lim_{n\to\infty} T(\mathcal{U}_n) = \mathcal{U}_0 + \lim_{n\to\infty} \left(\alpha_n \frac{\partial T_2}{\partial \alpha}(\xi_n) \right)$$

for some $\xi_n \in (0, \alpha_n)$. Since ξ_n is positive, we can bound $\partial T_2/\partial\alpha$ independently of n:

$$\frac{\partial T_2}{\partial \alpha}(\xi_n) < 1 - \gamma_2,$$

which implies

$$\mathcal{U}^* < \mathcal{U}_0 + (1-\gamma_2) \lim_{n\to\infty} \alpha_n = \mathcal{U}_0 + (1-\gamma_2)\alpha^* < \infty$$

as desired. ∎

COROLLARY 3.2. *Suppose $\gamma_2 = \epsilon^t$ for $0 < t < 1$ and $\gamma_1 = \epsilon^s$ for $t < s < 1 + t$. Then the assumptions of Theorem 3.1 are met, and hence the conclusions follow.*

Under an additional technical assumption on the locations γ_1 and γ_2, we next show the algorithm from Section 3.3 will converge rapidly in the present simplified setting. So long as the tolerance $\tau = \mathcal{O}(\epsilon^2)$, we show the algorithm will converge after just one iteration.

THEOREM 3.2. *Let α_0 and α_1 be the first two entries of the sequence from Definition 3.9. As in Corollary 3.2, assume $\gamma_2 = \epsilon^t$ for $1/2 < t < 1$ and $\gamma_1 = \epsilon^s$ for $t < s < 1 + t$, and additionally assume that $s > (t+1)/3$. Then*

$$\lim_{\epsilon \downarrow 0} \frac{\alpha_1 - \alpha_0}{\epsilon^2} = 0.$$

Proof. By definition $\alpha_1-\alpha_0=T_1(\mathcal{U}_1)-T_0(\mathcal{U}_0)$; from the mean value theorem

$$\alpha_1-\alpha_0=(\mathcal{U}_1-\mathcal{U}_0)\frac{\partial T_1}{\partial \mathcal{U}}(\xi)$$

for some $\xi\in(\mathcal{U}_0,\mathcal{U}_1)$. Let

$$b(z):=\frac{\gamma_1^2-1-2\gamma_1 z}{\gamma_1-1-z}$$

(compare to (3.8)). Then

$$\alpha_1-\alpha_0=[b(\alpha_0)-b(0)](\gamma_2-1)\frac{\partial T_1}{\partial \mathcal{U}}(\xi).$$

Since $(\gamma_2-1)\to 1$ as $\epsilon\to 0$, we analyze only $(b(\alpha_0)-b(0))\partial T_1/\partial\mathcal{U}(\xi)$; with the aid of the computer algebra system Sage [53], we first write its denominator as:

$$\begin{aligned}&\big(\epsilon\gamma_1^2\gamma_2+M\epsilon\gamma_2^2+\tilde{B}_3\gamma_1\gamma_2^2-\tilde{B}_3\gamma_2^3-M\epsilon\gamma_2-2\tilde{B}_3\gamma_1\gamma_2-2\epsilon\gamma_1\gamma_2+2\tilde{B}_3\gamma_2^2\\&\quad+\epsilon\gamma_2^2+\tilde{B}_3\gamma_1+\overline{B}_2\gamma_2-\tilde{B}_3\gamma_2+\gamma_1\gamma_2-\gamma_2^2-\overline{B}_2-\gamma_1+\gamma_2\big)\\&\quad\times\big(M\epsilon\gamma_2+2\epsilon\gamma_1\gamma_2-\epsilon\gamma_2^2+B_3\xi+B_2-\xi\big)^2.\end{aligned}$$

Of the quantities in the first set of parentheses, γ_2 is asymptotically the largest for vanishing ϵ. Since $\xi\in(\mathcal{U}_0,\mathcal{U}_1)$ and $\mathcal{U}_0=\gamma_2(1+\gamma_1-\gamma_2-\gamma_1/\gamma_2)$, ξ is at least asymptotically similar to γ_2. Thus we can say that in total the denominator is at least asymptotically similar to γ_2^3.

The numerator of $(b(\alpha_0)-b(0))\partial T_1/\partial\mathcal{U}(\xi)$ equals

$$\begin{aligned}&\big(-\tilde{B}_3\epsilon\gamma_1^2+2\tilde{B}_3\epsilon\gamma_1\gamma_2-\tilde{B}_3\epsilon\gamma_2^2+\epsilon\gamma_1^2+M\epsilon\gamma_2+\overline{B}_2\big)\\&\qquad\times\big(M\epsilon\gamma_2+\tilde{B}_3\gamma_1\gamma_2+\epsilon\gamma_1\gamma_2-\tilde{B}_3\gamma_2^2-\tilde{B}_3\gamma_1+\tilde{B}_3\gamma_2\\&\qquad-\gamma_1\gamma_2+\overline{B}_2+\gamma_1\big)(\gamma_1-\gamma_2)(\gamma_1-1)\gamma_2.\end{aligned}\tag{3.19}$$

To prove the desired result, it suffices to show that (3.19) divided by $\gamma_2^3\epsilon^2$ limits to zero for vanishing ϵ, meaning

$$\lim_{\epsilon\downarrow 0}\frac{q_1^\epsilon q_2^\epsilon(1-\gamma_2)(\gamma_1/\gamma_2-1)}{\gamma_2\epsilon^2}=0$$

where

$$\begin{aligned}q_1^\epsilon&=-\tilde{B}_3\epsilon\gamma_1^2+2\tilde{B}_3\epsilon\gamma_1\gamma_2-\tilde{B}_3\epsilon\gamma_2^2+M\epsilon\gamma_2+\epsilon\gamma_1^2+\overline{B}_2\\q_2^\epsilon&=\big(M\epsilon\gamma_2+\tilde{B}_3\gamma_1\gamma_2+\epsilon\gamma_1\gamma_2-\tilde{B}_3\gamma_2^2-\tilde{B}_3\gamma_1+\tilde{B}_3\gamma_2-\gamma_1\gamma_2+\overline{B}_2+\gamma_1\big).\end{aligned}$$

Since γ_1 is the asymptotically largest term in q_2^ϵ, the result will follow if $q_1^\epsilon\gamma_1/(\gamma_2\epsilon^2)\to 0$ as $\epsilon\searrow 0$. Since $M=H\epsilon$ and the bound B.3 shows that $\tilde{B}_3$ is asymptotically similar to ϵ, the first four terms in q_1^ϵ vanish faster than ϵ^2. The assumption in the theorem statement that $s>(t+1)/3$ ensures the fifth term in q_1^ϵ additionally vanishes. Finally, observe that σ_ϵ in (B.1) is asymptotically similar to $\epsilon^{1/2+3t/2}$, so that by (B.2) $\overline{B}_2$ must vanish faster than ϵ^{1+2t}. Since $t>1/2$, the result follows. ∎

4. Numerical results

We now present two-dimensional numerical tests of the HMM scheme in situations both where the periodic homogenization theory is applicable and where it is not. All computations are performed using the open source finite element (FEM) package FEniCS [37, 38], and all meshes are generated using Gmsh [27]. In the first four cases considered, $\epsilon = 0.025$ and $|\Omega^{\text{mac}}| = \mathcal{O}(1)$, and $\nu = 1$. Different values are prescribed for the final example of a backwards facing step and are detailed below. In all cases, the parameter defining the upper boundary of the microscopic domain $\gamma = 4\epsilon$.

All discretizations are performed with the Taylor-Hood elements, i.e. P_2 and P_1 basis functions for the velocity and pressure fields, respectively [31, 36], and the resulting discrete nonlinear system is solved with Newton's method, using the solution to the corresponding Stokes problem as the initial guess.

As in any multiscale method, the accurary of the HMM scheme depends not only on the fine-scale parameter ϵ but also the mesh size of the macro and microscale solvers. In particular, the microscale mesh spacing h must tend to zero faster than ϵ for convergence; see, for example, the fully discrete analysis of a finite-element based HMM scheme for multiscale elliptic equations in [1]. Although a fully discrete analysis is out of the scope of the present work, consider briefly an approximation of the microscale velocity u by P_k elements. Standard FEM estimates give that the approximation error in the H^1 norm is proportional to $h^k \|u\|_{H^{k+1}}$. If one assumes the asymptotic scaling (2.4) for u, then $\|u\|_{H^{k+1}}$ scales as $1/\epsilon^k$. Thus, one must have $h/\epsilon \to 0$ for vanishing ϵ. All of the microscale simulations described below respect this requirement.

The direct numerical simulation (DNS) of the full problem (2.2) is computed with a large number of elements and is compared with (i) the 1st order approximation satisfying the no-slip condition along Γ (so-called because of (2.3)) and (ii) the HMM approximation satisfying the coupled system (3.4); the 1st order approximation and macroscale HMM function are both computed on the same mesh. The coupled HMM system is solved iteratively, using the algorithm from Section 3.3. The tolerance τ for the error between successive slip amounts α is set to be $\tau = \epsilon^2$.

4.1. Flow in a channel with periodic roughness. First consider a channel domain with periodic roughness, as in Figure 4.1a. The macroscopic domain is simply $\Omega^{\text{mac}} = [0,1]^2$, and the roughness is parameterized by the function $\varphi^\epsilon(x_1) = \epsilon/2(\cos(2\pi x_1/\epsilon) - 1)$. The no-slip condition is applied at the upper boundary $x_2 = 1$, and periodic boundary conditions are applied on the left/right boundaries. A constant pressure gradient $-\nabla p = (1\ 0)^T$ drives the flow from left to right.

In the setting just described, the macroscopic solution U is one dimensional. Only the horizontal component of the flow is nonzero, and it depends only on the wall-normal variable x_2. In this case, only one micro-domain is needed, and periodic boundary conditions can be prescribed along the left/right computational boundaries of the micro-domain ($x_1 = 0$ and $x_1 = \epsilon$) for simplicity, as discussed in Remark 3.4. The free stream condition (3.6) is then applied along the upper computational boundary $x_2 = \gamma = 4\epsilon$.

In this setting of a domain with periodic side walls, there is a small difficulty using the FEniCS software package whose workaround we briefly describe. As mentioned, the mixed P_2–P_1 finite elements are used to numerically solve the stationary Navier-Stokes system in Ω^{mic}.

The discrete equations posed with Dirichlet condtions for the velocity vector u along $\partial\Omega^{\text{mic}}_{\text{noslip}}$ and $x_2 = \gamma$ and periodic conditions at the side-walls have a unique solution from the standard finite element theory. The pressure field exists to (weakly) enforce incompressibility and does not formally satisfy any boundary conditions. For mixed

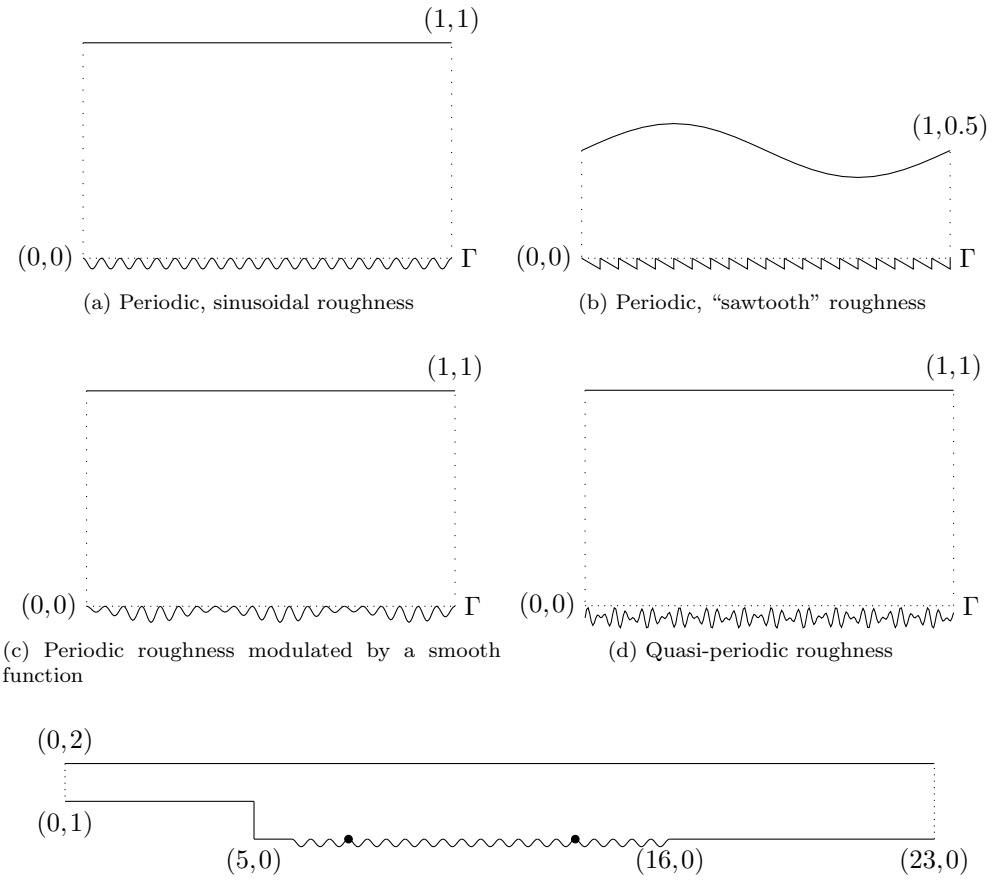

(a) Periodic, sinusoidal roughness

(b) Periodic, "sawtooth" roughness

(c) Periodic roughness modulated by a smooth function

(d) Quasi-periodic roughness

(e) Backwards facing step with roughness in the recirculation region. The two dots mark the locations of the micro-domains discussed in Section 4.5.

FIG. 4.1. *Sketches of the rough domains used to test the numerical method.*

finite element methods however FEniCS requires that either *both* function spaces or *neither* have periodic boundaries. Since we want the velocity u to be periodic for $x_2 \in [0,\gamma]$, we consequently assume the microscale pressure can be written as $p = p_{\text{per}} + \tilde{p}$, where p_{per} is periodic and $-\nabla\tilde{p} = (1\ 0)^T$ is a body force that is consistent with the macroscopic forcing driving the flow throughout the channel. We then compute the solution pair (u, p_{per}). Whenever periodic boundary conditions are imposed at $x_1 = s$ and $x_1 = s + L^{\text{mic}}$ in the descriptions below, this decomposition is used.

Figures 4.2 and 4.3 plot u_1 and $\partial u_1/\partial x_2$, respectively, as functions of x_1 for several values of x_2 near the wall. Also computed was an HMM solution using the more general strategy for the projection operator π defined by the constraints detailed in Appendix A (not pictured). The resulting slip amount differed from the one computed with periodic boundary conditions in the micro domain only by 0.9%.

4.2. Nonsquare domain with periodic roughness. Next, consider a nonsquare macroscopic domain with periodic, "sawtooth" roughness as shown in Figure

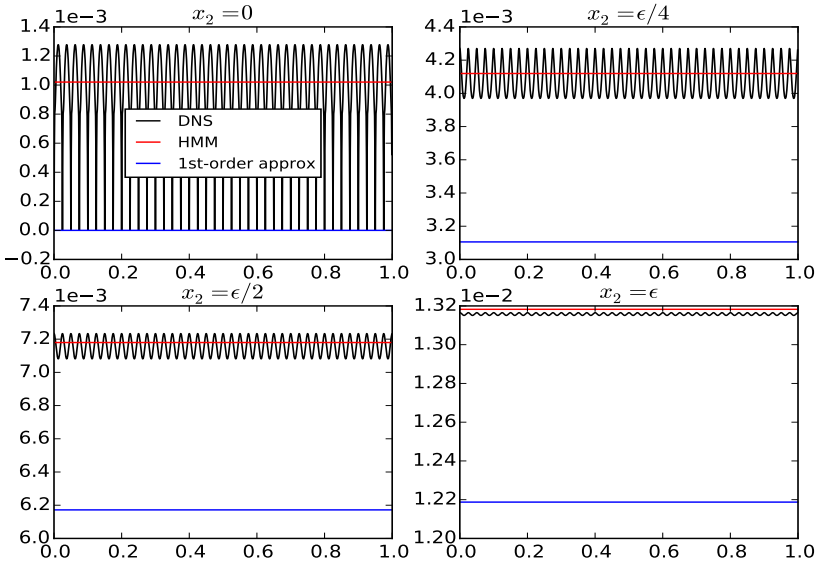

FIG. 4.2. *Horizontal component of the flow u_1 versus x_1 plotted at various heights x_2 for the domain shown in Figure 4.1a.*

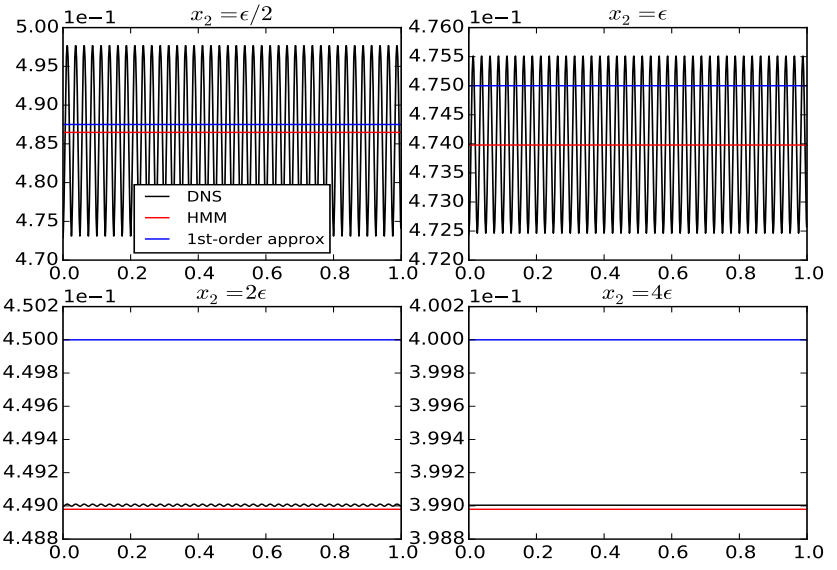

FIG. 4.3. *Shear $\partial u_1/\partial x_2$ versus x_1 plotted at various heights x_2 for the domain shown in Figure 4.1a.*

4.1b. Let $h(x_1) := 0.5 - 0.125\sin(2\pi x_1)$. Then

$$\Omega^{\text{mac}} = \{(x_1, x_2) | 0 \le x_1 \le 1,\ 0 \le x_2 \le h(x_1)\}.$$

The roughness is parameterized by the periodic function $\varphi^\epsilon(x_1) = -3\epsilon/4(x_1/\epsilon - \lfloor x_1/\epsilon \rfloor)$, where $\lfloor \cdot \rfloor$ denotes the floor function. The no-slip condition is applied on the domain's upper, curved boundary, and periodic boundary conditions are applied on the left/right boundaries. A constant body force $f = (1\ 0)^T$ drives the flow from left to right.

To compute the HMM approximations, we use the algorithm from Section 3.3 and set

$$\{s_1, s_2, s_3, s_4, s_5\} = \{0, 0.25, 0.5, 0.75, 1\}$$

chosen to capture influence of the macroscopic curvature of Ω^{mac}. However, the percent difference between the largest and smallest resulting values of slip amounts is a negligible 0.3%, indicating that simply performing one micro-solve at a single s_j is sufficient in this case.

In contrast to the previous example, the macroscopic flow U is not one dimensional, i. e. both U_2 and $\partial U_1/\partial x_1$ are nonzero, as can be seen from the DNS curve in Figures 4.4 and 4.5. However, since at $x_2 = 4\epsilon$ the horizontal component of the flow is approximately one order of magnitude larger than the vertical component for a given x_1, it is reasonable to attempt to approximate the vertical component as being zero and compute with periodic boundary conditions and the free-stream condition (3.6). Similar to the previous numerical example in Section 4.1, a difference of about one percent is observed between the slip amount computed this way and the slip amount using the more general projection $\pi_j(U)$ from Appendix A. The results in Figures 4.4 and 4.6 again show u_1 and $\partial u_1/\partial x_2$ versus x_1 for various values of x_2.

4.3. Flow in a channel with non-periodic roughness. Consider again $\Omega^{\text{mac}} = [0,1]^2$, but now let the roughness be parameterized by

$$\begin{aligned}
\zeta^\epsilon(x_1) &= \beta(x_1)\varphi^\epsilon(x_1) \\
\beta(x_1) &= \sin^2\left(\sqrt{2}2\pi x_1\right) + 0.5 \\
\varphi^\epsilon(x) &= \epsilon/2(\cos(2\pi x_1/\epsilon) - 1),
\end{aligned}$$

so that the periodic roughness is modulated by a smooth function as shown in Figure 4.1c. The no-slip condition is applied at $x_2 = 1$, periodic boundary conditions are enforced at $x_1 = 0$ and $x_1 = 1$, and a uniform pressure gradient $-\nabla p = (1\ 0)^T$ again drives the flow from left to right.

The algorithm from Section 3.3 is used with

$$\{s_1, s_2, s_3, s_4, s_5, s_6, s_7\} = \{0, 0.15, 0.35, 0.525, 0.675, 0.875, 0.975\}$$

chosen to capture the large scale curvature of β. The asymptotic analysis presented in Section 2.2 suggests it is sufficient to simply compute in a single microscopic domain with roughness parameterized only by φ^ϵ and then multiply the resulting slip amount by $\beta(x_1)$ in the effective boundary condition (3.1). However, we chose to apply the general HMM algorithm to mimic the situation for which an analytic formula for β is not known. The total slip amount used in the macroscale domain is a linear interpolation of the α_j, $1 \le j \le 7$.

In this case, the percent difference between the largest and smallest slip amounts is a non-negligible 23.4%. Figures 4.7 and 4.8 illustrate HMM's successful capturing of the slip amount's horizontal dependence.

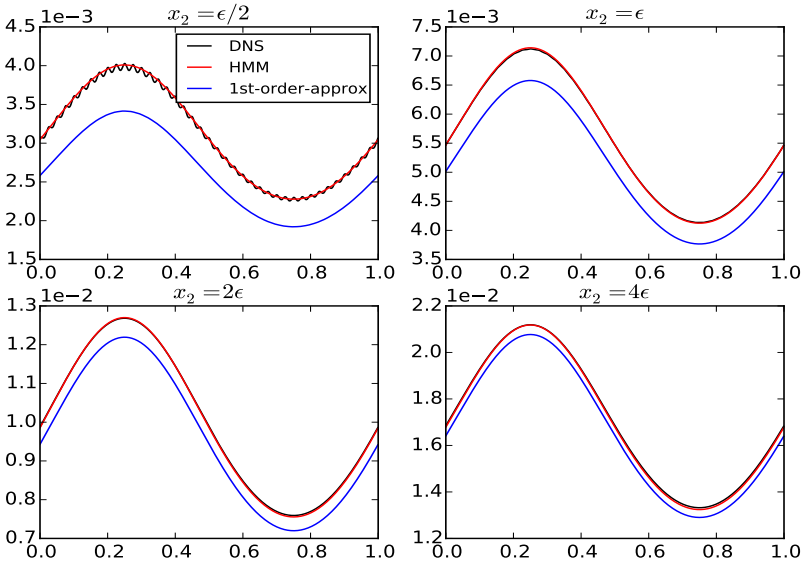

FIG. 4.4. *Horizontal component of the flow u_1 versus x_1 plotted at various heights x_2 for the domain shown in Figure 4.1b.*

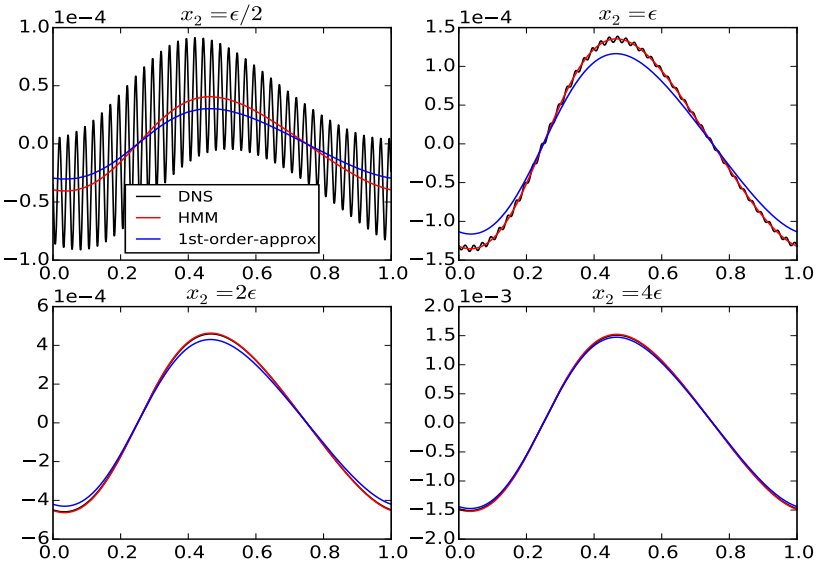

FIG. 4.5. *Vertical component of the flow u_2 versus x_1 plotted at various heights x_2 for the domain shown in Figure 4.1b; compared to u_1 in Figure 4.4, u_2 is roughly one order of magnitude smaller.*

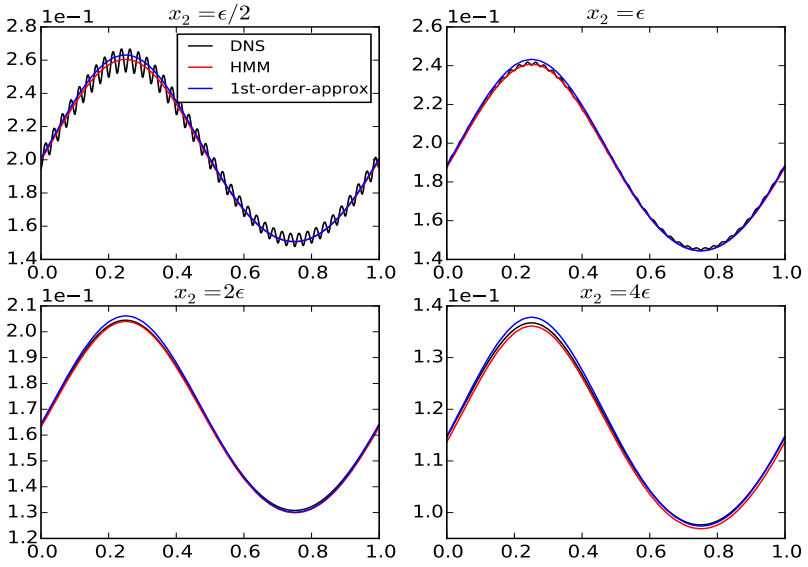

FIG. 4.6. *Shear $\partial u_1/\partial x_2$ versus x_1 plotted at various heights x_2 for the domain shown in Figure 4.1b.*

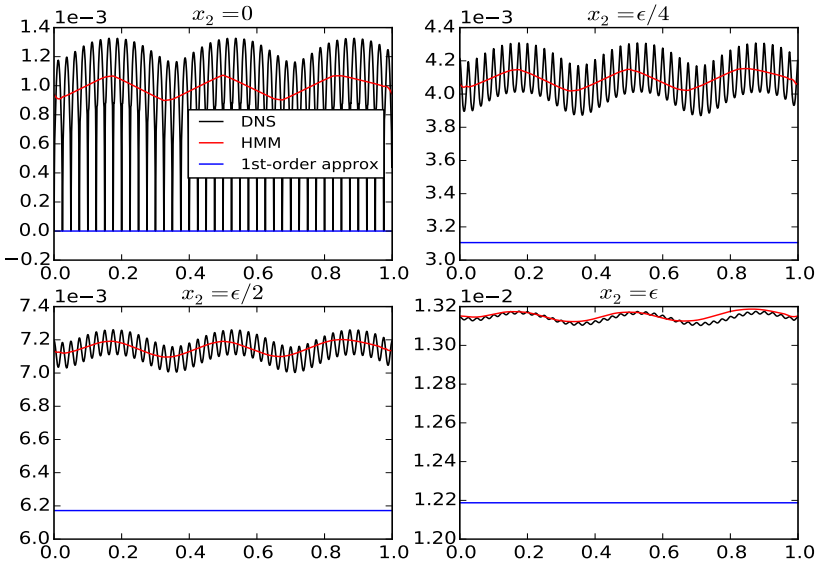

FIG. 4.7. *Horizontal component of the flow u_1 versus x_1 plotted at various heights x_2 for the domain shown in Figure 4.1c.*

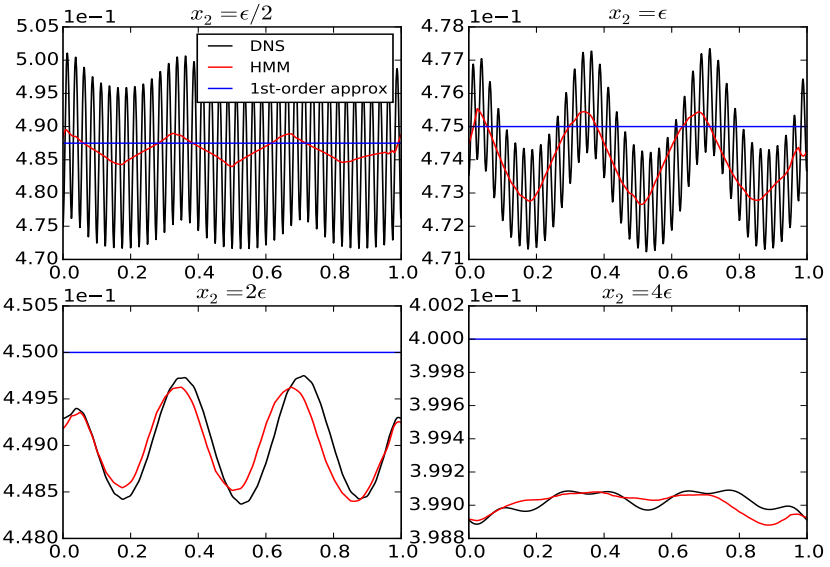

FIG. 4.8. *Shear $\partial u_1/\partial x_2$ versus x_1 plotted at various heights x_2 for the domain shown in Figure 4.1c.*

4.4. Flow in a channel with quasi-periodic roughness. Consider now a rough boundary parameterized by the quasi-periodic function

$$\varphi^\epsilon(x_1) = \epsilon/3\left(\sin(\sqrt{2}\cdot 2\pi x_1/\epsilon) + \sin(2\pi x_1/\epsilon) - 2.25\right),$$

like the one displayed in Figure 4.1d. As in Sections 4.1 and 4.3, $\Omega^{\text{mac}} = [0,1]^2$, and no-slip is applied at $x_2 = 0$. For both Ω^ϵ and Ω^{mac}, periodic boundary conditions are applied at $x_1 = 0$ and $x_1 = 1$. For u^ϵ this is only an approximation, since φ^ϵ is not truly periodic, which explains the spurious boundary layers in the DNS solution near $x_1 = 0$ and $x_1 = 1$, as seen in Figures 4.9 and 4.10.

The same problem is encountered in the micro-domain if periodic boundary conditions are prescribed. Instead, we use the Dirichlet boundary conditions described in Appendix A for the projection operator π_j. In this case the no-slip condition is applied at the locations $(s_j, \varphi^\epsilon(s_j))$ and $(s_j + L_j^{\text{mic}}, \varphi^\epsilon(s_j + L_j^{\text{mic}}))$. In more general situations such as this where the microscale roughness is no longer periodic, it is best to take each $L_j^{\text{mic}} > \epsilon$ in order to capture a few "correlation lengths" of φ^ϵ. The results shown in Figures 4.9 and 4.10 are performed with a single micro domain at $s = 0.481561$ and length $L^{\text{mic}} = 5\epsilon$.

We note also that if one still wants to use periodic boundary conditions for the microscale computation another option is to further increase the horizontal domain length L and then replace the smoothing operator from Definition 3.4 with

$$\langle u \rangle_L (x,y) = \int_x^{x+L} K(s) u(s,y)\, ds$$

where K is smooth function that has compact support, integrates to unity, and satisfies some vanishing moment conditions. Such kernels are well known in the numerical homogenization community [9,23,28] and likely would be useful in more realistic applications beyond the academic test cases presented here.

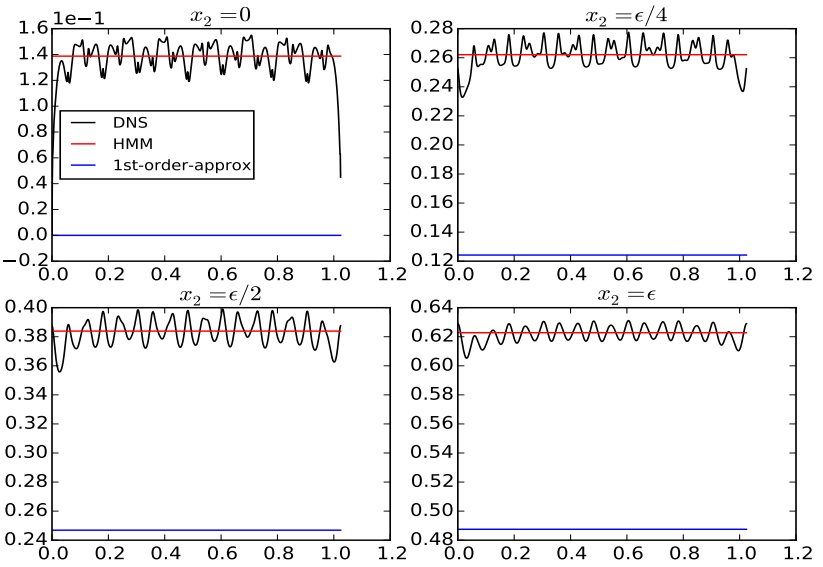

FIG. 4.9. *Horizontal component of the flow u_1 versus x_1 plotted at various heights x_2 for the domain shown in Figure 4.1d.*

4.5. Flow over a backwards facing step. Consider now flow over a backwards facing step with periodic roughness after the step, as in Figure 4.1e. The roughness is parameterized by the function

$$\varphi^\epsilon(x) = \epsilon/2\,(\cos(2\pi x_1/\lambda) - 1),$$

similar to Section 4.1 but with a larger wavelength $\lambda = 2.5\epsilon$. We are primarily interested in the effect of the roughness on the flow after the step. Hence for simplicity there is no roughness in the inflow region prior to the step, and the roughness does not cover the full horizontal extent of the domain. In this case, both viscosity $\nu = 0.1$ and $\epsilon = 0.1$, and the horizontal length of the domain is $L = 23$. A Poiseuille inflow profile drives the flow, and the Reynolds number based on the profile is $Re = 150$. At this value, some recirculation after the step is expected. A zero-stress condition is applied at the outflow $x_1 = 23$: $\nu\nabla u - pI = 0$, and for both the full DNS solution and the 1st order approximation, the no-slip condition is applied on all other domain boundaries. The HMM solution, of course however satisfies the slip condition (3.1).

The algorithm from Section 3.3 is used with two points $\{s_1, s_2\} = \{7.5, 13.5\}$ (marked with black dots in Figure 4.1e) chosen to lie (i) closer to the step, and hence within the recirculation bubble, and (ii) farther away from the step, after the bubble. Given $\{\alpha_1, \alpha_2\}$ at these micro domain locations, the slip amount is given as a piecewise linear

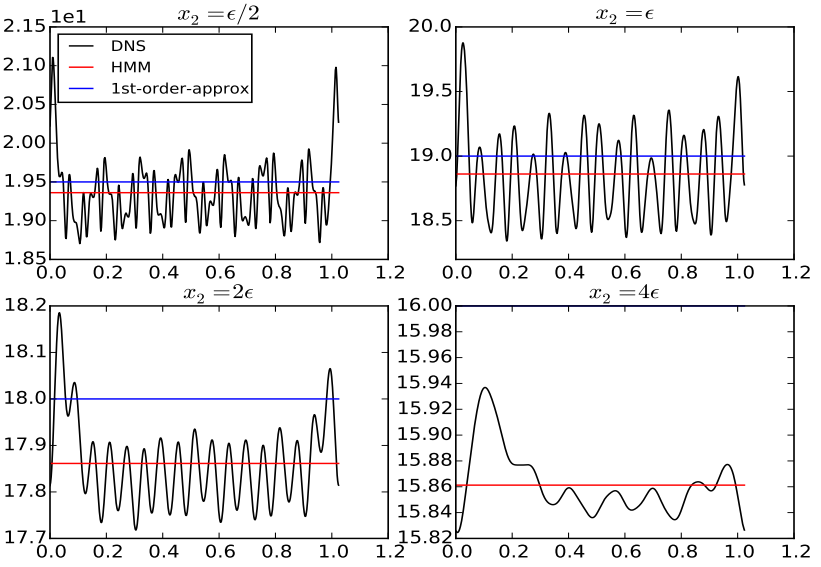

FIG. 4.10. *Shear $\partial u_1/\partial x_2$ versus x_1 plotted at various heights x_2 for the domain shown in Figure 4.1d.*

interpolant

$$\alpha(x_1) = \mathbb{1}_{[6,16]}(x_1)\mathcal{I}_{\text{linear}}((6,0),(7.5,\alpha_1),(13.5,\alpha_2),(16,0))(x_1) \tag{4.1}$$

where $\mathbb{1}$ is the indicator function, and $x_1 = 6$ and $x_1 = 16$ are the points at which the roughness begins and ends, and hence before and after which there should be no-slip. In retrospect a piecewise constant interpolant $\mathcal{I}_{\text{constant}}$ in the region $6 \le x_1 \le 16$ would be more appropriate, since (4.1) does not capture the slip amount as far out in x_1 as it should. Another option would be to simply perform micro simulations at more points $s_j \in [6,16]$ along the roughness.

In this case the more general projection operator $\pi_j(U)$ from Appendix A is applied in both micro-domains. Because of the fluid recirculation, there is a nontrivial mass flux along the upper computational boundary $x_2 = \gamma = 4\epsilon$ of the micro-domain at $s_1 = 7.5$. This results in a 10.2% difference in the slip amounts computed at $s_1 = 7.5$ and $s_2 = 13.5$, even though the roughness pattern is the same. As a result, the HMM solution correctly captures the effect of roughness on the size of the recirculation bubble, something the 1st-order approximation fails to do. Figures 4.11 and 4.12 thus illustrate the utility of constraining the micro-domains to match the local macroscopic solution.

4.6. Discussion. In all cases, the HMM solution computed with the algorithm from Section 3.3 is a clear improvement over the 1st-order, no-slip approximation; it captures the average effect of roughness on the flow. Although not displayed in the examples above, separate HMM solutions were also computed by calculating a slip

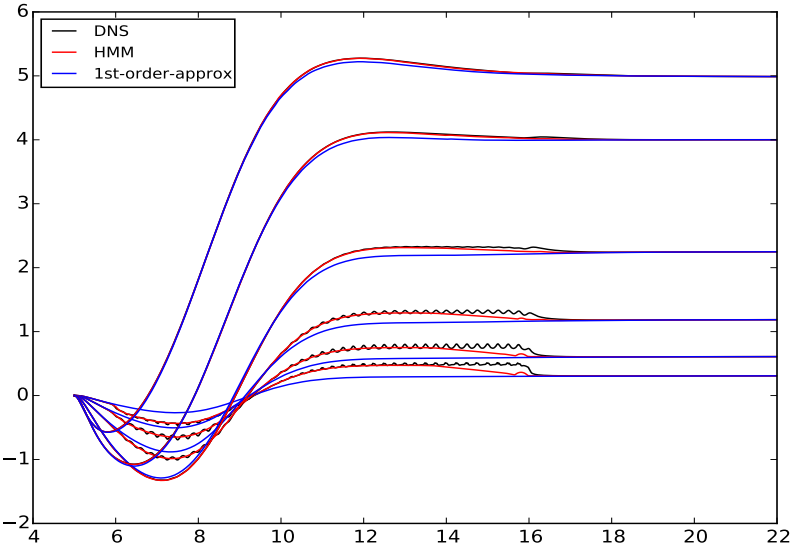

FIG. 4.11. *Horizontal component of the flow* u_1 *versus* x_1 *plotted at the values* $x_2 = \epsilon/4, \epsilon/2, \epsilon, 2\epsilon, 4\epsilon, 0.55$ *for the domain shown in Figure 4.1e.*

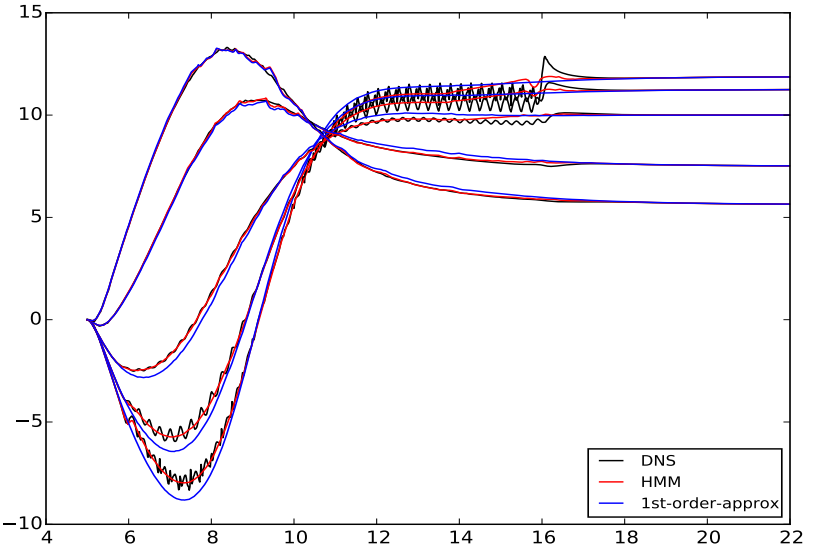

FIG. 4.12. *Shear* $\partial u_1/\partial x_2$ *versus* x_1 *plotted at the values* $x_2 = \epsilon/2, \epsilon, 2\epsilon, 4\epsilon, 0.55$ *for the domain shown in Figure 4.1e.*

length at height $x_2 = h > 0$

$$\alpha_{j,h} = \frac{\langle u_1^j \rangle_{L_j^{\text{mic}}}(s_j, h)}{\langle \partial u_1^j / \partial x_2 \rangle_{L_j^{\text{mic}}}(s_j, h)}.$$

The slip amount fed back to the macro-solver was then defined to be

$$\alpha_j = \alpha_{j,h} - h, \tag{4.2}$$

based on a simple linear extrapolation of $\langle u_1^j \rangle$ from $x_2 = h$ to $x_2 = 0$. We experimented with both $h = \epsilon$ and $h = 2\epsilon$ and found that (4.2) differed from α_j computed with (3.5) by at most a few percent.

As mentioned at the beginning of Section 4, the 1st-order approximation satisfying the no-slip condition along Γ and the HMM solution are both computed on the same discretization of Ω^{mac}. For the first four numerical examples presented in Sections 4.1–4.4, this amounts to approximately 4%–6% of the mesh cells used to discretize Ω^ϵ. After accounting for the mesh cells used to discretize each Ω_j^{mic}, the HMM solution is computed on about 8%–19% of the mesh cells used to compute the full, oscillatory solution u^ϵ for the parameters described at the beginning of Section 4. Generally speaking, the cost of the micro-solvers depends on the macroscopic variations of the rough boundary Γ_ϵ as well as the correlation length of the oscillations. The former affects the *number* of micro-domain solutions J while the latter affects the *size* of each Ω_j^{mic}.

In principle, the computational cost of computing each micro-domain solution is indepedent of ϵ, since the domain size scales with ϵ. The computational savings afforded by solving for the HMM solution instead of the full, rough-wall solution u^ϵ of course increase as ϵ decreases relative to the measure of Ω^{mac}. For the backwards facing step problem described in Section 4.5, the system parameters were chosen to highlight the effect of the roughness on the size of the recirculation bubble. For the selected parameters, the total mesh cells for the HMM solution was actually about 20% more than the mesh cells for u^ϵ. For decreasing ϵ, this situation would reverse, but the rough-wall's influence on the macroscopic flow patterns would be less prominent.

Finally, note that in each of the numerical examples presented, the slope of the roughness profiles ζ^ϵ was $\mathcal{O}(1)$. We additionally conducted simulations of flow over roughness with slopes $\mathcal{O}(\epsilon)$ and $\mathcal{O}(1/\epsilon)$, as analyzed rigorously in [11] and [7], respectively; however, we found that the no-slip condition and viscous effects made the effective slip amount negligible in these cases. We found a similarly negligible effect from adding higher frequencies to the roughness profiles; for example, for periodic φ, the slip amount observed from roughness of the form $\zeta^\epsilon(x_1) = \epsilon\varphi(x_1/\epsilon) + \epsilon^2\varphi(x/\epsilon^2)$ was essentially the same as for $\zeta^\epsilon(x_1) = \epsilon\varphi(x_1/\epsilon)$.

5. Conclusions and future directions

We develop computational techniques for computing effective boundary conditions for laminar, viscous flow over a rough surface. The technique is based on coupling a 'macroscale' solver M in a large domain with smooth boundary to one or more 'microscale' solvers m localized to the the rough surface. The microscale solvers estimate the slip amount in the wall-law utilized by the macrosolver. The coupling strategy is described in the framework of the heterogeneous multiscale method (HMM). So long as the surface roughness is asymptotically small relative to the size of the full domain, the method is designed to efficiently capture the average effect of surface roughness on the flow for arbitrary roughness patterns. Numerical examples illustrate the method's utility for a variety of cases.

We prove the coupled system is consistent for linear Stokes flow in a channel with periodic roughness; starting from a no-slip Poiseuille flow, a back-and-forth iteration will converge to a fixed point. Moreover, we show the convergence happens rapidly– the difference between the slip amounts after the first and second iteration is smaller than $\mathcal{O}(\epsilon^2)$, where ϵ is the small-scale parameter characterizing the surface roughness. Finally, we show the HMM slip amount vanishes as ϵ vanishes, so that the macroscale HMM flow and the true, rough-wall flow u^ϵ both converge to the same quantity, namely, Poiseuille flow with no-slip condition posed on a smooth boundary. A future challenge remains, however, to rigorously estimate the difference between the HMM approximation and u^ϵ, either by adapting the currently available homogenization techniques [33, 34, 43] or by inventing new ones.

Laminar incompressible flow over a bed of porous media is a setting analogous to the current one; future work could build off the studies of [35] and [54] and analyze a HMM that couples local micro-solvers based on Darcy's law to Navier-Stokes macro-solvers for the large-scale flow. In that case, mathematically rigorous results also exist that suggest the form of the wall-law at the interface of the fluid and porous media [32].

For numerous other boundary layer problems in fluid mechanics however there does *not* exist any rigorous theory describing an effective boundary condition that captures the system's asymptotic dynamics. The present work offers some indication that a computational approach based on coupling macro and microscale simulations could be successfully used to numerically derive wall-laws in such cases.

One example is wall-bounded electrokinetic flows. In the presence of charged surfaces, an asymptotically thin charge layer forms [50, 52]. This layer is the primary source of both momentum and charge transport for such flows; for flows relevant to microfluidics, however, its physics is poorly represented by continuum models. An HMM approach would couple a relatively efficient continuum solver M for the bulk flow to a molecular model m for the near-wall charge layer [18, 47]. One challenge is representing the effect of thermal fluctuations in both macro and microscale simulations in a consistent way [20].

Another example is wall-bounded turbulent flow; when the friction Reynolds number is large enough, there is a clear separation of scales between the near-wall eddies and those in the bulk flow [51]. Based on this observation, Sandham et al. coupled a large eddy simulation (LES) to a sequence of micro-solvers localized to the wall in which direct numerical simulation (DNS) was performed [49]. In the language of HMM, the coupling was done concurrently, or 'on-the-fly'. In [15] we built on this approach and further developed the local DNS solvers for use in a sequential multiscale framework, i.e. so that precomputed information could be utilized by a macroscale LES. More work is needed to design a wall-law for an LES that can use such information [46]. Intermittency remains a formidable obstacle.

Acknowledgments. The authors thank Yoonsang Lee for discussions regarding the heterogeneous multiscale method, Matthew Novack for discussions regarding the proof of the technique's convergence to a fixed point, and the anonymous referees for their helpful suggestions and comments. The authors acknowledge support from the Oden Institute for Computational Engineering and Sciences and National Science Foundation Grant DMS-1620396.

Appendix A. Boundary conditions for micro-scale systems. In more general situations in which the macroscopic flow has nontrivial dependence on x_1 and/or a nontrivial vertical component, a more general approach is needed than the "free-stream" condition mentioned in Remark 3.4. We propose to prescribe quadratic Dirichlet condi-

tions for both the horizontal and vertical components of the velocity along each of the three faces of $\partial\Omega_{j,\mathrm{D}}^{\mathrm{mic}}$ (those that intersect $x_1 = s_j$, $x_1 = s_j + \epsilon$ and $x_2 = \gamma$). Let

$$\begin{aligned}
\Gamma_1^{\mathrm{mic}} &= \{(x_1, x_2) | 0 \le x_2 \le \gamma, x_1 = s_j\} \\
\Gamma_2^{\mathrm{mic}} &= \{(x_1, x_2) | s_j \le x_1 \le s_j + L_j^{\mathrm{mic}}, x_2 = \gamma\} \\
\Gamma_3^{\mathrm{mic}} &= \{(x_1, x_2) | 0 \le x_2 \le \gamma, x_1 = s_j + L_j^{\mathrm{mic}}\}
\end{aligned}$$

be the left, upper, and right computational boundaries of the micro-domain (the dependence of each Γ^{mic} on j is implied). Then there are two quadratic profiles for each boundary, each with three coefficients to be determined, and hence 18 total constraints are needed. Let u_k and v_k be the quadratic profile for the horizontal and vertical component of the flow at Γ_k^{mic}, $k = 1,2,3$. The no-slip requirement (3.3) gives four constraints

$$0 = u_1(s_j, 0) = v_1(s_j, 0) = u_3(s_j + L_j^{\mathrm{mic}}, 0) = v_3(s_j + L_j^{\mathrm{mic}}, 0).$$

Additionally, enforce that the mass flux across each Γ_k^{mic} is the same as the macroscopic mass flux

$$\begin{aligned}
\int_{\Gamma_1^{\mathrm{mic}}} u_1 \, ds &= \int_{\Gamma_1^{\mathrm{mic}}} U \cdot n \, ds \\
\int_{\Gamma_2^{\mathrm{mic}}} v_2 \, ds &= \int_{\Gamma_2^{\mathrm{mic}}} U \cdot n \, ds \\
\int_{\Gamma_3^{\mathrm{mic}}} u_3 \, ds &= \int_{\Gamma_3^{\mathrm{mic}}} U \cdot n \, ds.
\end{aligned} \tag{A.1}$$

Since U is divergence-free, these imply conservation of mass along the micro-domain boundaries

$$\int_{\Gamma_1^{\mathrm{mic}}} u_1 \, ds + \int_{\Gamma_2^{\mathrm{mic}}} v_2 \, ds + \int_{\Gamma_3^{\mathrm{mic}}} u_3 \, ds = 0,$$

hence satisfying requirement (3.2). Equations (A.1) hence give three more conditions. To completely specify the quadratic profiles, one more condition each is needed for u_1 and u_3, two more conditions are needed for v_1, v_2, and v_3, and three conditions are needed for u_2. For continuity, enforce the interpolation constraints

$$\begin{aligned}
u_1(s_j, \gamma) = u_2(s_j, \gamma) &= U(s_j, \gamma) \cdot e_1 \\
v_1(s_j, \gamma) = v_2(s_j, \gamma) &= U(s_j, \gamma) \cdot e_2 \\
u_2(s_j + L_j^{\mathrm{mic}}, \gamma) = u_3(s_j + L_j^{\mathrm{mic}}, \gamma) &= U(s_j + L_j^{\mathrm{mic}}, \gamma) \cdot e_1 \\
v_2(s_j + L_j^{\mathrm{mic}}, \gamma) = v_3(s_j + L_j^{\mathrm{mic}}, \gamma) &= U(s_j + L_j^{\mathrm{mic}}, \gamma) \cdot e_2,
\end{aligned}$$

which leaves one more condition each for v_1, u_2, and v_3. Adding one more interpolation point for each

$$\begin{aligned}
v_1(s_j, \gamma/2) &= U(s_j, \gamma/2) \cdot e_2 \\
u_2(s_j + L_j^{\mathrm{mic}}/2, \gamma) &= U(s_j + L_j^{\mathrm{mic}}/2, \gamma) \cdot e_1 \\
v_3(s_j + L_j^{\mathrm{mic}}, \gamma/2) &= U(s_j + L_j^{\mathrm{mic}}, \gamma/2) \cdot e_2.
\end{aligned}$$

ensures the Dirichlet conditions are thus uniquely determined along each Γ_k^{mic}, which then completely defines a projection operator π_j.

Appendix B. Estimates for Stokes flow. By definition

$$\overline{B}_2 = \int_0^\epsilon u_2(x_1,0)\,dx$$

meaning

$$|\overline{B}_2| \le \int_0^\epsilon |u_2(x_1,0)|\,dx \le \|u_2\|_{L^1} \le |\Omega_{\text{mic}}|^{1/2}\,\|u_2\|_{L^2} \le [(M+\gamma_2)\epsilon]^{1/2}\,\|u_2\|_{H^1}.$$

By the Lax-Milgram theorem [8], we know

$$\|u_2\|_{H^1} \le (2+C_p^2)\,\|g_2\|_{H^1},$$

where C_p is the Poincaré constant (which is estimated in Appendix C) and g_2 is the (nonunique) pre-image of the trace-map Tr of the boundary values for u_2:

$$\text{Tr}(u_2) = \begin{cases} 0, & x_2 = \gamma_2 \\ -u_1\big|_{\Gamma_\epsilon}, & (x_1,x_2) \in \Gamma_\epsilon. \end{cases}$$

Let

$$\begin{aligned} g_2(x_1,x_2) = m(x_1)(x_2-\gamma_2) &= \left(\frac{u_1\big(-\varphi^\epsilon(x_1)\big)}{\gamma_2+\varphi^\epsilon(x_1)}\right)(x_2-\gamma_2) \\ &= \left(\frac{-(M-\varphi^\epsilon(x_1))(\varphi^\epsilon(x_1)+\gamma_2)}{\gamma_2+\varphi^\epsilon(x_1)}\right)(x_2-\gamma_2), \end{aligned}$$

then $g_2(x_1,\gamma_2)=0$ and $g_2(x_1,-\varphi^\epsilon(x_1)) = -u_1(-\varphi^\epsilon(x_1))$, i.e. $\text{Tr}(\text{g}_2) = \text{Tr}(\text{u}_2)$. The gradient is

$$\frac{\partial g_2}{\partial x_1} = \frac{\partial m}{\partial x_1}(x_2-\gamma_2) = \varphi'(x_1/\epsilon)(x_2-\gamma_2)$$

and

$$\frac{\partial g_2}{\partial x_2} = m(x_1) = \frac{u_1\big(-\varphi^\epsilon(x_1)\big)}{\gamma_2+\varphi^\epsilon(x_1)}.$$

Measuring each term in the H^1 norm:

$$\begin{aligned} \|g_2\|_{L^2}^2 &= \int_0^\epsilon \int_{-\varphi^\epsilon(x_1)}^{\gamma_2} \big(m(x_1)\big)^2 (x_2-\gamma_2)^2\,dx_2\,dx_1 \\ &= \frac{1}{3}\int_0^\epsilon \big(m(x_1)\big)^2 (\varphi^\epsilon(x_1)+\gamma_2)^3\,dx_1 \\ &= \frac{1}{3}\int_0^\epsilon \big[u_1\big(-\varphi^\epsilon(x_1)\big)\big]^2 (\varphi^\epsilon(x_1)+\gamma_2)\,dx_1 \\ &\le \frac{1}{3}\,\epsilon(M\gamma_2)^2(M+\gamma_2) \end{aligned}$$

since $u_1(\varphi^\epsilon)$ is largest at $y=0$ and $\varphi^\epsilon(x) \le M$.

$$\|\partial g_2/\partial x_1\|_{L^2}^2 = \int_0^\epsilon \int_{-\varphi^\epsilon(x_1)}^{\gamma_2} \big(\varphi'(x_1/\epsilon)\big)^2 (x_2-\gamma_2)^2\,dx_2\,dx_1$$

$$
\begin{aligned}
&= \frac{1}{3}\int_0^{\epsilon} \left(\varphi'(x_1/\epsilon)\right)^2 \left(\varphi^{\epsilon}(x_1)+\gamma_2\right)^3 dx_1 \\
&\leq \frac{1}{3}\epsilon (M+\gamma_2)^3 \left\|\varphi'\right\|_{\infty}^2 .
\end{aligned}
$$

Finally,

$$
\begin{aligned}
\left\|\partial g_2/\partial x_2\right\|_{L^2}^2 &= \int_0^{\epsilon}\int_{-\varphi^{\epsilon}(x_1)}^{\gamma_2} \left(m(x_1)\right)^2 dx_2\, dx_1 \\
&= \int_0^{\epsilon} \frac{\left(u_1\left(-\varphi^{\epsilon}(x_1)\right)\right)^2}{\gamma_2+\varphi^{\epsilon}(x_1)}\, dx_2\, dx_1 \\
&\leq \frac{1}{\gamma_2}\int_0^{\epsilon} \left(u_1\left(-\varphi^{\epsilon}(x_1)\right)\right)^2 dx_1 \\
&\leq \frac{\epsilon}{\gamma_2}\left(M\gamma_2\right)^2 = \epsilon\gamma_2 M^2 .
\end{aligned}
$$

Putting it all together:

$$
\left\|g_2\right\|_{H^1} \leq \left[\frac{1}{3}\epsilon(M\gamma_2)^2(M+\gamma_2)+\frac{1}{3}\epsilon(M+\gamma_2)^3\left\|\varphi'\right\|_{\infty}^2+\epsilon\gamma_2 M^2\right]^{1/2} =: \sigma_{\epsilon}, \tag{B.1}
$$

so that in total

$$
|\overline{B}_2| \leq (2+C_p^2)[(M+\gamma_2)\epsilon]^{1/2}\sigma_{\epsilon}. \tag{B.2}
$$

Next we bound $\tilde{B}_3$. By definition

$$
\tilde{B}_3 = \int_0^{\epsilon} \tilde{u}_3(x_1,0)\, dx_1
$$

meaning

$$
|\tilde{B}_3| \leq \int_0^{\epsilon} |\tilde{u}_3(x_1,0)|\, dx_1 \leq \left\|\tilde{u}_3\right\|_{L^1} \leq |\Omega_{\text{mic}}|^{1/2}\left\|\tilde{u}_3\right\|_{L^2} \leq [(M+\gamma_2)\epsilon]^{1/2}\left\|\tilde{u}_3\right\|_{H^1} .
$$

Again we know by the Lax-Milgram theorem [8] that

$$
\left\|\tilde{u}_3\right\|_{H^1} \leq (2+C_p^2)\left\|g_3\right\|_{H^1} ,
$$

where g_3 is the pre-image of the trace-map Tr of the boundary values for $\tilde{u}_3$:

$$
\text{Tr}(\tilde{u}_3) = \begin{cases} 1, & x_2 = \gamma_2 \\ 0, & (x_1,x_2) \in \Gamma_{\epsilon}. \end{cases}
$$

Let

$$
g_3(x_1,x_2) = \begin{cases} x_2/\gamma_2, & (x_1,x_2) \in [0,\epsilon]\times[0,\gamma_2] \\ 0, & (x_1,x_2) \in \Omega_{\text{mic}} \setminus [0,\epsilon]\times[0,\gamma_2]. \end{cases}
$$

Then

$$
\left\|g_3\right\|_{H^1}^2 = \int_0^{\epsilon}\int_0^{\gamma_2} \left(x_2^2+1\right)/\gamma_2^2\, dx_2\, dx_1 = \epsilon\left(\frac{\gamma_2}{3}+\frac{1}{\gamma_2}\right)
$$

meaning

$$|\tilde{B}_3| \leq (2+C_p^2)[(M+\gamma_2)\epsilon]^{1/2}\|g_3\|_{H^1} = \epsilon[(M+\gamma_2)]^{1/2}(2+C_p^2)\left(\frac{\gamma_2}{3}+\frac{1}{\gamma_2}\right)^{1/2}. \quad \text{(B.3)}$$

Appendix C. Estimate for Poincaré constant. The bounds (B.2) and (B.3) both depend on the Poincaré constant C_p, i.e. the constant such that

$$\|u\|^2_{L^2(\Omega^{\text{mic}})} \leq C_p^2\|\nabla u\|^2_{L^2(\Omega^{\text{mic}})} \qquad \forall u \in \mathcal{H}$$

where

$$\mathcal{H} = \{\psi \in H^1(\Omega^{\text{mic}}) : \psi|_{\Gamma_\epsilon} = \psi|_{x_2=\gamma_2} = 0,\ \psi \text{ is periodic at } x_1 = 0 \text{ and } x_1 = \epsilon\}.$$

We now show $C_p \to 0$ as $\epsilon \searrow 0$, which is necessary to determine the asymptotic character of $\overline{B}_2$ and $\tilde{B}_3$.

Let $u \in \mathcal{H}$. For $x_1 \in [0,\epsilon)$, we know from direct computation of the spectrum of the operator $-\partial^2/\partial x_2^2$ acting on the interval $[-\varphi^\epsilon(x_1),\gamma_2]$ with homogeneous Dirichlet boundary conditions that

$$\int_{-\varphi^\epsilon(x_1)}^{\gamma_2} |u(x_1,x_2)|^2\,dx_2 \leq \left(\frac{L_y(x_1)}{\pi}\right)^2 \int_{-\varphi^\epsilon(x_1)}^{\gamma_2} \left|\frac{\partial u}{\partial x_2}(x_1,x_2)\right|^2 dx_2$$

where $L_y(x_1) = \gamma_2 + \varphi^\epsilon(x_1) \leq \gamma_2 + M$. Integrating both sides of the inequality from $x_1 = 0$ to $x_1 = \epsilon$ then gives

$$\begin{aligned}\|u\|^2_{L^2(\Omega^{\text{mic}})} &\leq \left(\frac{\gamma_2+M}{\pi}\right)^2 \left\|\frac{\partial u}{\partial x_2}\right\|^2_{L^2(\Omega^{\text{mic}})} \\ &\leq \left(\frac{\gamma_2+M}{\pi}\right)^2 \|\nabla u\|^2_{L^2(\Omega^{\text{mic}})} \qquad \text{(C.1)}\end{aligned}$$

so that indeed $C_p \to 0$ as $\epsilon \searrow 0$ as desired.

REFERENCES

[1] A. Abdulle, *On a priori error analysis of fully discrete heterogeneous multiscale FEM*, Multiscale Model. Simul., 4(2):447–459, 2005. 4

[2] A. Abdulle, E. Weinan, B. Engquist, and E. Vanden-Eijnden, *The heterogeneous multiscale method*, Acta Numer., 21:1–87, 2012. 1, 2.3

[3] Y. Achdou, *Effet d'un mince revêtement métallisé mince sur la réflexion d'une onde électromagnetique*, C.R. Acad. Sci. Paris Sér. I, 314(3):217–222, 1992. 1

[4] Y. Achdou and O. Pironneau, *Analysis of wall laws*, C.R. Acad. Sci. Paris Ser. I, 320:541–547, 1995. 1, 2

[5] Y. Achdou, O. Pironneau, and F. Valentin, *Effective boundary conditions for laminar flows over periodic rough boundaries*, J. Comput. Phys., 147(1):187–218, 1998. 1, 2, 2, 2.2, 2.1, 2.2, 3.2, 3.4

[6] Y. Achdou, P. Le Tallec, F. Valentin, and O. Pironneau, *Constructing wall laws with domain decomposition or asymptotic expansion techniques*, Comput. Meth. Appl. Mech. Engrg., 151:215–232, 1998. 1, 2

[7] Y. Amirat, O. Bodart, U.D. Maio, and A. Gaudiello, *Effective boundary condition for Stokes flow over a very rough surface*, J. Differ. Equ., 254(8):3395–3430, 2013. 1, 2, 4.6

[8] T. Arbogast and J.L. Bona, *Method of Applied Mathematics*, University of Texas at Austin, 2008. B, B

[9] D. Arjmand and O. Runborg, *A time dependent approach for removing the cell boundary error in elliptic homogenization problems*, J. Comput. Phys., 314:206–227, 2016. 4.4
[10] M. Artola and M. Cessenat, *Diffraction d'une onde electromagnetique par une couche composite mince accolee a un conducteur epais*, C.R. Acad. Sci. Paris Ser. I, 313:231–236, 1991. 1
[11] A. Basson and D. Gérard-Varet, *Wall laws for fluid flows at a boundary with random roughness*, Commun. Pure Appl. Math., 61(7):941–987, 2008. 1, 2, 2, 2.2, 4.6
[12] A. Bottaro and S.B. Naqvi, *Effective boundary conditions at a rough wall: a high-order homogenization approach*, Meccanica, 55:1781–1800, 2020. 1
[13] D. Bresch and D. Gérard-Varet, *Roughness-induced effects on the quasi-geostrophic model*, Commun. Math. Phys., 253(1):81–119, 2005. 1
[14] D.M. Bushnell and K.J. Moore, *Drag reduction in nature*, Annu. Rev. Fluid Mech., 23(1):65–79, 1991. 1
[15] S.P. Carney, B. Engquist, and R.D. Moser, *Near-wall patch representation of wall-bounded turbulence*, J. Fluid Mech., 903:A23, 2020. 5
[16] A. Carrau, P. Letallec, and G. Gallice, *Taking into account surface roughness in computing hypersonic re-entry flows*, Proceedings of the 10th International Conference on Computing Methods in Applied Sciences and Engineering, 331–343, 1991. 1
[17] A.L. Dalibard and D. Grard-Varet, *Effective boundary condition at a rough surface starting from a slip condition*, J. Differ. Equ., 251(12):3450–3487, 2011. 1, 2
[18] L.D. Site, M. Praprotnik, J.B. Bell, and R. Klein, *Particle-continuum coupling and its scaling regimes: Theory and applications*, Adv. Theory Simul., 3(5):1900232, 2020. 5
[19] G. Deolmi, W. Dahmen, and S. Müller, *Effective boundary conditions: A general strategy and application to compressible flows over rough boundaries*, Commun. Comput. Phys., 21(2):358–400, 2017. 1
[20] A. Donev, J.B. Bell, A.L. Garcia, and B.J. Alder, *A hybrid particle-continuum method for hydrodynamics of complex fluids*, Multiscale Model. Simul., 8(3):871–911, 2010. 5
[21] W. E and B. Engquist, *The heterogeneous multiscale methods*, Commun. Math. Sci., 1(1):87–132, 2003. 2.3
[22] W. E, B. Engquist, X. Li, W. Ren, and E. Vanden-Eijnden, *Heterogeneous multiscale methods: A review*, Commun. Comput. Phys., 2:367–450, 2007. 1, 2.3
[23] B. Engquist and Y.-H. Tsai, *Heterogeneous multiscale methods for stiff ordinary differential equations*, Math. Comput., 74(252):1707–1742, 2005. 4.4
[24] E. Friedmann, *The optimal shape of riblets in the viscous sublayer*, J. Math. Fluid. Mech., 12:243–265, 2010. 1
[25] E. Friedmann and T. Richter, *Optimal microstructures drag reducing mechanism of riblets*, J. Math. Fluid. Mech., 13(3):429–447, 2011. 1
[26] D. Gérard-Varet, *Highly rotating fluids in rough domains*, J. Math. Pures Appl., 82(11):1453–1498, 2003. 1
[27] C. Geuzaine and J.-F. Remacle, *Gmsh: A 3-D finite element mesh generator with built-in pre- and post-processing facilities*, Inter. J. Numer. Meth. Eng., 79(11):1309–1331, 2009. 4
[28] A. Gloria, *Reduction of the resonance error. Part 1: Approximation of homogenized coefficients*, Math. Model. Meth. Appl. Sci., 21(8):1601–1630, 2011. 4.4
[29] W.W. Grabowski, *Coupling cloud processes with the large-scale dynamics using the cloud-resolving convection parameterization (CRCP)*, J. Atmos. Sci., 58(9):978–997, 2001. 2.3
[30] I. Grooms and A.J. Majda, *Efficient stochastic superparameterization for geophysical turbulence*, Proc. Natl. Acad. Sci., 110(12):4464–4469, 2013. 2.3
[31] M.D. Gunzburger, *Finite Element Methods for Viscous Incompressible Flows: A Guide to Theory, Practice, and Algorithms*, Academic Press, 1989. 4
[32] W. Jäger and A. Mikelić, *On the interface boundary condition of beavers, joseph, and saffman*, SIAM J. Appl. Math, 60(4):1111–1127, 2000. 1, 5
[33] W. Jäger and A. Mikelić, *On the roughness-induced effective boundary conditions for an incompressible viscous flow*, J. Differ. Equ., 170(1):96–122, 2001. 1, 2, 2, 2.2, 5
[34] W. Jäger and A. Mikelić, *Couette flows over a rough boundary and drag reduction*, Commun. Math. Phys., 232:429–455, 2003. 1, 2, 2, 2.2, 5
[35] U. Lācis and S. Bagheri, *A framework for computing effective boundary conditions at the interface between free fluid and a porous medium*, J. Fluid Mech., 812:866–889, 2017. 1, 5
[36] W. Layton, *Introduction to the Numerical Analysis of Incompressible Viscous Flows*, SIAM, Philadelphia, PA, USA, 2008. 4
[37] A. Logg, K.-A. Mardal, and G.N. Wells, *Automated Solution of Differential Equations by the Finite Element Method*, Springer, 2012. 4
[38] A. Logg, G.N. Wells, and J. Hake, *DOLFIN: a C++/Python Finite Element Library*, in A. Logg, K.A. Mardal, and G. Wells (eds.), Automated Solution of Differential Equations by the Finite

Element Method, Springer, 173–225, 2012. 4
[39] A.J. Majda, *Multiscale models with moisture and systematic strategies for superparameterization*, J. Atmos. Sci., 64(7):2726–2734, 2007. 2.3
[40] A.J. Majda and M.J. Grote, *Mathematical test models for superparameterization in anisotropic turbulence*, Proc. Natl. Acad. Sci., 106(14):5470–5474, 2009. 2.3
[41] A.J. Majda and I. Grooms, *New perspectives on superparameterization for geophysical turbulence*, J. Comput. Phys., 271:60–77, 2014. 2.3
[42] A. Mikelić, *Rough boundaries and wall laws*, in E. Feireisl, P. Kaplicky, J. Malek (Eds.), Qualitative Properties of Solutions to Partial Differential Equations, Lect. Notes Necas Center Math. Modeling, vol. 5, Matfyzpress, Publishing House of the Faculty of Mathematics and Physics Charles University in Prague, Prague, 103–134, 2009. 1
[43] A. Mikelić, Šarka Nečasová, and Maria Neuss-Radu, *Effective slip law for general viscous flows over an oscillating surface*, Math. Meth. Appl. Sci., 36(15):2086–2100, 2013. 1, 5
[44] C.B. Millikan, *A critical discussion of turbulent flows in channels and circular tubes*, Proceedings of the fifth International Congress for Applied Mechanics, 386–392, 1938. 1
[45] J. Pedlosky, *Geophysical Fluid Dynamics*, Springer-Verlag New York, 1987. 1
[46] U. Piomelli and E. Balaras, *Wall-layer models for large-eddy simulations*, Annu. Rev. Fluid Mech., 34(1):349–374, 2002. 1, 5
[47] W. Ren and W. E, *Heterogeneous multiscale method for the modeling of complex fluids and microfluidics*, J. Comput. Phys., 204(1):1–26, 2005. 2.3, 5
[48] W. Ren and W. E, *Boundary conditions for the moving contact line problem*, Phys. Fluids, 19(2):022101, 2007. 2.3
[49] N.D. Sandham, R. Johnstone, and C.T. Jacobs, *Surface-sampled simulations of turbulent flow at high Reynolds number*, Int. J. Numer. Meth. Fluids, 85(9):525–537, 2017. 5
[50] O. Schnitzer and E. Yariv, *Macroscale description of electrokinetic flows at large zeta potentials: Nonlinear surface conduction*, Phys. Rev. E, 86:021503, 2012. 1, 5
[51] A.J. Smits and I. Marusic, *Wall-bounded turbulence*, Phys. Today, 66(9):25–30, 2013. 5
[52] T.M. Squires and M.Z. Bazant, *Induced-charge electro-osmosis*, J. Fluid Mech., 509:217–252, 2004. 1, 5
[53] W.A. Stein et al., *Sage Mathematics Software (Version 7.5.1)*, The Sage Development Team, 2017. 3.4
[54] Y. Sudhakar, U. Lācis, S. Pasche, and S. Bagheri, *Higher-order homogenized boundary conditions for flows over rough and porous surfaces*, Transp. Porous Med., 136:1–42, 2021. 1, 2, 5
[55] R. Temam, *Navier Stokes Equations: Theory and Numerical Analysis*, AMS Chelsea Publishing, 1984. 3.4